Digital Predistortion for Power Amplifier Linearization in Radar-Communication Shared Apertures

A Complexity and Robustness Study of Memoryless and Generalized Memory Polynomial Models

Master's thesis in Wireless, Photonics and Space Engineering

Måns Müntzing

Department of Electrical Engineering
CHALMERS UNIVERSITY OF TECHNOLOGY

Gothenburg, Sweden 2026
www.chalmers.se

Master's thesis 2026

Digital Predistortion for Power Amplifier Linearization in Radar-Communication Shared Apertures

A Complexity and Robustness Study of Memoryless and Generalized Memory Polynomial Models

Måns Müntzing

CHALMERS
UNIVERSITY OF TECHNOLOGY

Department of Electrical Engineering
Communication, Antennas and Optical Networks
Chalmers University of Technology
Gothenburg, Sweden 2026

Digital Predistortion for Power Amplifier Linearization in Radar-Communication Shared Apertures
A Complexity and Robustness Study of Memoryless and Generalized Memory Polynomial Models
Måns Müntzing

Supervisor: Niklas Janehag, Saab AB
Supervisor: Henrik Helmius, Saab AB
Supervisor: Filip Aldebrink, Saab AB
Examiner: Jian Yang, Electrical Engineering

Master's Thesis 2026
Electrical Engineering
Communication, Antennas and Optical Networks
Chalmers University of Technology
SE-412 96 Gothenburg
Telephone +46 31 772 1000

Typeset in LaTeX
Gothenburg, Sweden 2026

Digital Predistortion for Power Amplifier Linearization in Radar-Communication Shared Apertures
A Complexity and Robustness Study of Memoryless and Generalized Memory Polynomial Models
MÅNS MÜNTZING
Department of Electrical Engineering
Chalmers University of Technology

Abstract

Shared radar and communication apertures are commonly optimized with radar performance as the primary design objective. As a result, transmitter operating conditions such as output power and amplifier efficiency are often chosen in a way that is sub-optimal for communication performance. In particular, operating a power amplifier close to compression improves efficiency and radar signal-to-noise ratio, but introduces nonlinear distortion that degrades communication metrics.

This thesis investigates the use of digital predistortion as a software-based linearization technique for communication signals transmitted through commonly utilized radar power amplifiers. Two amplifier models are considered: a memoryless Saleh model representing a traveling-wave tube amplifier (TWTA), and a generalized memory polynomial (GMP) model representing a solid-state power amplifier (SSPA) with nonlinear memory effects. Four communication waveforms are evaluated: two single carrier waveforms and two orthogonal frequency-division multiplexing (OFDM) waveforms. Digital predistortion models are trained using an indirect learning architecture and assessed in terms of linearization performance, model complexity, robustness to noise, and sensitivity to amplifier mismatch.

The results show that digital predistortion can significantly reduce nonlinear distortion without requiring changes to the radio frequency hardware. For the memoryless TWTA model, a low-complexity memoryless polynomial predistorter provides sufficient linearization performance. For the memory-dependent SSPA model, memory depth is the dominant factor affecting performance, especially for OFDM-based waveforms. Polynomial order and cross terms provide additional improvements, but with diminishing returns. Further analysis also shows that the predistortion models are robust to moderate noise and amplifier variations, although the SSPA model case is more sensitive to nonlinear memory mismatch. Overall, the thesis demonstrates that digital predistortion is a promising approach for improving communication performance in shared radar-communication transmitter systems.

Keywords: digital predistortion, power amplifier linearization, generalized memory polynomial, TWTA, SSPA, radar-communication systems, EVM, ACLR, NMSE

Acknowledgements

I would like to express my sincere gratitude to Saab AB for the opportunity to undertake this master's thesis, as well as for providing valuable insight into the company and its values.

I am also deeply grateful to my supervisors at Saab, Niklas, Henrik, and Filip, for their guidance, valuable input, and support throughout the project. Their advice and encouragement have been greatly appreciated, and I am especially thankful for the welcoming and inclusive environment they helped create.

Måns Müntzing, Gothenburg, June 2026

List of Acronyms

The acronyms used throughout this thesis are listed below in alphabetical order:

ACLR	Adjacent Channel Leakage Ratio
AM/AM	Amplitude Modulation to Amplitude Modulation
AM/PM	Amplitude Modulation to Phase Modulation
AWGN	Additive White Gaussian Noise
BER	Bit Error Rate
BPSK	Binary Phase-Shift Keying
CFO	Carrier Frequency Offset
CP	Cyclic Prefix
DFT-s	Discrete Fourier Transform Spread
DPD	Digital Predistortion
EVM	Error Vector Magnitude
FFT	Fast Fourier Transform
GMP	Generalized Memory Polynomial
IFFT	Inverse Fast Fourier Transform
ILA	Indirect Learning Architecture
LS	Least Squares
LUT	Look-Up-Table
MP	Memory Polynomial
NMSE	Normalized Mean Square Error
OFDM	Orthogonal Frequency Division Multiplexing
P1dB	1 dB Compression Point
PA	Power Amplifier
PAPR	Peak-to-Average Power Ratio
PSD	Power Spectral Density
QAM	Quadrature Amplitude Modulation
QPSK	Quadrature Phase-Shift Keying
RF	Radio Frequency
RLS	Recursive Least Squares
RMS	Root Mean Square
RRC	Root-Raised Cosine

SNR	Signal-to-Noise Ratio
SSPA	Solid-State Power Amplifier
TWTA	Traveling-Wave Tube Amplifier
WOLA	Weighted Overlap-and-Add

Contents

List of Figures

List of Tables

1
Introduction

In systems where a shared aperture is used for both radar and communication purposes, radar performance is typically the primary design driver. Consequently, transmitter parameters such as operating point, linearity requirements, and spectral characteristics are often optimized to satisfy radar constraints. While this approach ensures radar functionality, it may render the aperture sub-optimal for communication purposes, thereby limiting the achievable communication link performance.

One primary optimization target is high transmitter output power, which is essential for achieving a high radar signal-to-noise ratio (SNR) and improving overall transmitter efficiency. In practice, this objective is constrained by the well-known linearity–efficiency trade-off in radio frequency (RF) power amplifiers (PAs) [1], [2]. To achieve high efficiency, PAs are often operated close to saturation or in the compression region. However, when a PA is driven near or beyond its linear operating region, the output power no longer increases proportionally with the input power. This nonlinear behavior is commonly described through amplitude modulation to amplitude modulation (AM/AM) and amplitude modulation to phase modulation (AM/PM) conversion [3], [4], and it leads to unwanted effects such as in-band distortion, constellation distortion, and spectral regrowth in the communication signal [5], [6].

Digital predistortion (DPD) is a well-established technique for mitigating nonlinear PA distortion [7]–[9]. By intentionally modifying the digital baseband signal prior to amplification, DPD compensates for the nonlinear transfer characteristics of the PA. When properly implemented, the cascade of the predistorter and the PA approximates an overall linear response. A wide range of behavioral models have been proposed for this purpose, including memory polynomial (MP) and generalized memory polynomial (GMP) models, which are particularly relevant when PA memory effects are significant [5], [6], [10]–[12]. DPD is therefore an important enabling technique in modern high-efficiency wireless transmitters, where stringent linearity and spectral-emission requirements must be met while maintaining high data rates [13], [14].

Compared with its maturity in communication transmitters, DPD has seen limited application in joint radar and communication apertures, particularly for DPD models capable of linearizing different types of amplifiers. Applying DPD in this context therefore has the potential to enable the use of more complex modulation schemes and thereby increase achievable data rates. Higher data rates allow information to be transmitted in shorter bursts, which can reduce the system's exposure time to interference and jamming and improve overall robustness.

1.1 Aim

The aim of this thesis is to develop and evaluate a DPD framework to mitigate PA nonlinearities in a communication link operating on a radar-optimized shared aperture.

The project will:
- Quantify communication performance degradation when the PA operates near or within compression.
- Develop a GMP behavioral model capturing AM/AM, AM/PM, and memory effects.
- Design and implement a DPD model to compensate for these nonlinearities.
- Evaluate improvements in error vector magnitude (EVM), adjacent channel leakage ratio (ACLR), and normalized mean square error (NMSE).
- Evaluate the model based on characterization needs and assess how removing certain parameters affects the model performance.

The objective is to assess whether software-based linearization can enable increased communication throughput without modification of the RF hardware.

1.2 Research questions

The research questions are divided into one primary research question and several secondary research questions. The primary research question defines the overall objective of the thesis, while the secondary research questions further specify the aspects of model complexity, waveform dependence, robustness, and generalization that are investigated.

1.2.1 Primary research question

What is the minimum-complexity DPD model that achieves acceptable linearization performance for radar-communication waveforms under nonlinear PA distortion and noise?

1.2.2 Secondary research questions

- **Model complexity:** How do GMP parameters, such as polynomial order, memory depth, and cross terms, affect linearization performance? Where is the point of diminishing returns?
- **Waveform dependence:** How do QAM, CP-OFDM, and DFT-s-OFDM waveforms differ in their DPD requirements? Does waveform PAPR correlate with the required model complexity?

- **Noise robustness:** How sensitive is the DPD performance to input noise and PA output or feedback noise? At what SNR does DPD become ineffective?
- **Model mismatch and generalization:** How well does a trained DPD model perform when the PA characteristics or operating conditions vary?
- **Complexity-performance trade-off:** What is the trade-off between the number of model parameters and performance metrics such as EVM, ACLR, and NMSE?

1.2.3 Definition of acceptable linearization performance

The considered radar-communication shared-aperture scenario is not tied to a specific communication standard. Therefore, no fixed external requirement is imposed for EVM, ACLR, or NMSE. Instead, acceptable linearization performance is defined relative to the achievable performance of the simulated system.

In this thesis, a DPD model is considered to provide acceptable linearization performance if it significantly improves the communication performance compared with the uncompensated PA case, while further increases in model complexity yield only marginal improvements. Marginal improvement is interpreted as less than approximately 1 dB improvement in NMSE or ACLR, or less than 0.5 percentage-point improvement in RMS EVM, when increasing the polynomial order, memory depth, or cross-term depth. The minimum-complexity model is therefore defined as the model with the fewest coefficients that reaches this performance plateau across the evaluated waveforms, or for a specific waveform when waveform-dependent model selection is considered.

1.3 Scope and limitations

The scope of this project is to analyze the nonlinearities in both solid-state (SSPA) and traveling-wave tube amplifiers (TWTA) when operating near and beyond the 1 dB compression point (P1dB), and to develop a suitable DPD model capable of compensating for these effects. The project further seeks to evaluate how DPD improves communication link metrics such as EVM, NMSE, and ACLR.

Due to confidentiality constraints related to the hardware, measured data from the operational system cannot be presented or directly utilized in this project. Consequently, the primary analysis is based on software behavioral models of power amplifiers and communication links. These models are designed to be sufficiently general and parameterized to enable straightforward adaptation and integration with real hardware in future implementations.

2

Theory

This chapter presents the theoretical background required to understand the modeling and linearization of nonlinear power amplifiers. First, the main nonlinear distortion mechanisms in power amplifiers are introduced. Then, behavioral modeling approaches are described, with particular focus on MP and GMP models. The chapter then discusses digital predistortion as a linearization technique and describes how model parameters can be estimated from measured data. Finally, the performance metrics used to evaluate the modeled and predistorted signals are defined.

2.1 Power Amplifier Nonlinearities

The two dominant forms of constellation distortion in power amplifiers are AM/AM distortion and AM/PM distortion. AM/AM distortion occurs when variations in the input amplitude produce nonlinear changes in the output amplitude, resulting in radial displacement of the constellation points. AM/PM distortion occurs when variations in the input amplitude introduce phase shifts in the output signal, causing angular rotation of the constellation points. Together, these nonlinear effects degrade modulation accuracy and increase the bit error rate (BER) [1], [4].

In a memoryless power amplifier model, the output signal $y[n]$ depends only on the instantaneous input signal $x[n]$, without considering past or future input samples. The model can therefore be expressed as

$$y[n] = f(x[n]), \tag{2.1}$$

where $f(\cdot)$ is an arbitrary nonlinear function [9], [15].

Moreover, in wideband PAs, the output signal depends not only on the current input sample but also on previous input samples due to dynamic effects in the amplifier. These memory effects arise from frequency-dependent behavior, bias circuits, thermal effects, and other electrical phenomena within the PA. Consequently, models with memory are required to accurately capture the nonlinear dynamic behavior of wideband power amplifiers [10]–[12], [16].

A general behavioral model with memory can be expressed as

$$y[n] = f(x[n], x[n-1], \ldots, x[n-M]), \tag{2.2}$$

where the output signal depends not only on the current input sample but also on the previous input samples up to the memory depth M. Here, $f(\cdot)$ represents an arbitrary nonlinear function describing both the nonlinear and dynamic behavior of the power amplifier [9], [15].

2.2 Behavioral Modeling of Power Amplifiers

Behavioral modeling is used to describe the input–output relationship of a power amplifier without requiring a detailed physical description of the internal device structure. Instead, the amplifier is represented by mathematical models that capture the dominant nonlinear and dynamic effects observed at the signal level. Such models are useful both for predicting amplifier distortion and for designing digital predistortion systems that compensate for this distortion [9], [15].

In this section, several commonly used behavioral models are presented, beginning with memoryless models such as the Saleh model and static polynomial model, followed by models with memory including Wiener, Hammerstein, Volterra-based, MP, and GMP models.

2.2.1 Memoryless models

The model presented in [3] has been widely used for power amplifier modeling due to its simplicity and its ability to accurately describe TWTAs. The Saleh model is memoryless, meaning that the output signal depends only on the current input sample and not on past or future inputs.

For a complex baseband input signal $x[n]$, the corresponding output signal $y[n]$ is given by

$$y[n] = A[n]e^{j(\psi[n]+\Phi[n])}, \tag{2.3}$$

where $\psi[n]$ denotes the phase of the input signal,

$$A[n] = \frac{\alpha_a |x[n]|}{1+\beta_a |x[n]|^2}, \tag{2.4}$$

and

$$\Phi[n] = \frac{\alpha_\Phi |x[n]|^2}{1+\beta_\Phi |x[n]|^2}. \tag{2.5}$$

The parameters α and β determine the characteristics of the model. The subscript a corresponds to the AM/AM conversion, while the subscript Φ corresponds to the AM/PM conversion. Consequently, the complete memoryless behavior of the TWTA can be characterized using four real-valued parameters.

Another commonly used memoryless behavioral model for power amplifiers is the static polynomial model [13], [15], which represents the nonlinear relationship between the input and output signals using a finite-order polynomial expansion. The model is given by

$$y[n] = \sum_{k=1}^{K} a(k)x[n]|x[n]|^{k-1}, \tag{2.6}$$

where K denotes the maximum polynomial order and $a(k)$ are the complex-valued polynomial coefficients describing the nonlinear characteristics of the amplifier.

2.2.2 Models with memory

A common simplification when modeling memory effects in power amplifiers is to assume that the dynamic behavior can be represented by linear filtering combined with a memoryless nonlinearity. In this case, the memory effects are modeled using linear convolutions together with a static nonlinear block [6], [17], [18].

A linear time-invariant filter can be expressed as

$$y[n] = \sum_{m=-\infty}^{\infty} h[m]x[n-m], \tag{2.7}$$

where $h[m]$ denotes the impulse response of the filter.

When the linear filter precedes the memoryless nonlinear block, the structure is referred to as a Wiener model. In this case, the filter determines how previous input samples influence the signal before the nonlinear operation. Conversely, when the linear filter follows the memoryless nonlinear block, the structure is called a Hammerstein model. Here, the nonlinear signal is shaped by the linear filter before generating the final output signal. Finally, when linear filters are placed both before and after the nonlinear block, the model is referred to as a Wiener–Hammerstein model. This structure captures both input-side and output-side dynamic effects surrounding the nonlinearity [6], [17], [18].

While Wiener and Hammerstein models provide intuitive block-oriented representations of nonlinear systems with memory, Volterra-based models offer a more general mathematical framework for behavioral PA modeling [15], [19].

2.2.2.1 Volterra-based models

The general nonlinear model with memory in (2.2) can be represented using a Volterra series [19]. A truncated discrete-time Volterra series is given by

$$y[n] = \sum_{k=1}^{K} \sum_{m_1=0}^{M-1} \cdots \sum_{m_k=0}^{M-1} h_k(m_1, \ldots, m_k) \prod_{l=1}^{k} x[n-m_l], \tag{2.8}$$

where K is the nonlinear order, M is the memory depth, and $h_k(m_1, \ldots, m_k)$ denotes the kth-order Volterra kernel. Each kernel describes how different delayed input samples interact to contribute to the output sample. Although the Volterra series is very general, it typically requires a large number of coefficients, which makes direct implementation computationally expensive [15], [19].

2.2.2.2 Memory Polynomial Model

A commonly used simplification of the Volterra series is the MP model. The MP model only includes diagonal Volterra terms and can be written as

$$y[n] = \sum_{k=1}^{K} \sum_{m=0}^{M} a(k,m) x[n-m] |x[n-m]|^{k-1}. \tag{2.9}$$

Here, K denotes the nonlinear order, M denotes the memory depth, and $a(k,m)$ are the complex-valued model coefficients [5], [16].

2.2.2.3 Generalized Memory Polynomial Model

The MP model can be further extended by incorporating cross terms between the signal and delayed or advanced envelope components. This yields the GMP model [6],

$$\begin{aligned} y[n] = &\sum_{k=1}^{K_a} \sum_{m=0}^{M_a} a(k,m) x[n-m] |x[n-m]|^{k-1} \\ &+ \sum_{k=1}^{K_b} \sum_{m=0}^{M_b} \sum_{l=1}^{L_b} b(k,m,l) x[n-m] |x[n-m-l]|^{k-1} \\ &+ \sum_{k=1}^{K_c} \sum_{m=0}^{M_c} \sum_{l=1}^{L_c} c(k,m,l) x[n-m] |x[n-m+l]|^{k-1}. \end{aligned} \tag{2.10}$$

In this model, the coefficients $a(k,m)$ describe the main memory polynomial terms, while $b(k,m,l)$ and $c(k,m,l)$ describe the lagging and leading cross terms, respectively. The parameters M_a, M_b, and M_c define the memory depths of the corresponding terms, while L_b and L_c define the lagging and leading cross-term depths.

2.3 Power Amplifier Technologies

The choice of behavioral model depends strongly on the amplifier technology, the signal bandwidth, and the operating region. Two commonly used PA technologies for joint radar-communication apertures are TWTAs and SSPAs. These differ in both their static nonlinear behavior and the significance of memory effects [2], [9].

TWTAs are often modeled using memoryless behavioral models, particularly in cases where memory effects are weak. One widely used example is the Saleh model, presented in (2.3). Due to its low complexity and ability to capture the dominant static nonlinearities, the Saleh model is well suited for simple TWTA characterization.

SSPAs, on the other hand, often exhibit more pronounced memory effects, especially when driven by wideband modulated signals. These memory effects arise from frequency-dependent behavior, biasing networks, thermal effects, and other dynamic mechanisms in the amplifier [6], [10], [11], [20]. Therefore, memoryless models are often insufficient for accurate SSPA characterization under wideband operation [6], [9].

As a result, behavioral models that include both nonlinear and dynamic effects are commonly used for SSPAs. In particular, MP and GMP models provide a practical trade-off between modeling accuracy and computational complexity, making them widely used for SSPA behavioral modeling and digital predistortion applications [5], [6], [9].

2.4 Digital Predistortion

DPD is a widely used technique for linearizing nonlinear power amplifiers. The principle is to modify the baseband signal before amplification so that the predistorter compensates for the nonlinear characteristics of the PA. Ideally, the predistorter approximates the inverse behavior of the amplifier, resulting in an approximately linear cascaded output [8], [9].

A simplified representation of this principle is

$$y[n] = f_{\mathrm{PA}}(f_{\mathrm{DPD}}(x[n]))\,, \tag{2.11}$$

where $x[n]$ is the original baseband input signal, $f_{\mathrm{DPD}}(\cdot)$ is the predistorter function, and $f_{\mathrm{PA}}(\cdot)$ is the PA function. The objective is to choose $f_{\mathrm{DPD}}(\cdot)$ such that

$$f_{\mathrm{PA}}(f_{\mathrm{DPD}}(x[n])) \approx Gx[n], \tag{2.12}$$

where G is the desired linear gain. In this way, the combined response of the predistorter and PA becomes approximately linear. The predistorter must therefore compensate for AM/AM and AM/PM distortion, and in wideband systems also for memory effects [6], [9].

2.4.1 Inverse Modeling

DPD is based on approximating the inverse behavior of the PA. For a memoryless amplifier, this inverse relationship can conceptually be written as

$$x[n] = f_{\mathrm{PA}}^{-1}(y[n]). \tag{2.13}$$

In practice, however, an exact analytical inverse is often difficult or impossible to obtain. For example, the Saleh model introduced in (2.3) contains nonlinear AM/AM and AM/PM characteristics that are not globally invertible over all operating regions. Practical PAs may also exhibit saturation and non-unique input–output mappings, which further limit the existence of an exact inverse [9].

Instead, DPD systems estimate an approximate inverse using behavioral models and measured input–output data. Polynomial-based models are commonly used for this purpose because they provide a practical balance between modeling accuracy and computational complexity [5], [6], [9].

2.4.2 DPD Model Structures

The behavioral models introduced for PA modeling can also be used for DPD, but with a different interpretation. In PA modeling, the model represents the forward mapping from PA input to PA output. In DPD, the same model structure is instead used to approximate the inverse mapping, generating a predistorted signal that compensates for the PA distortion [9], [21].

For amplifiers with weak memory effects, the static polynomial model in (2.6) can be used as a memoryless predistorter, where the coefficients are chosen to introduce inverse AM/AM and AM/PM characteristics. For amplifiers with significant memory effects, the memory polynomial model in (2.9) extends this compensation to nonlinear distortion that depends on previous input samples. The generalized memory polynomial model in (2.10) further includes lagging and leading cross terms, allowing more complex dynamic interactions to be modeled [5], [6].

Thus, the static polynomial, MP, and GMP structures can all be used either as forward PA models or as DPD models. When applied to DPD, the coefficients are estimated to approximate the inverse behavior of the PA rather than its forward response [9], [21].

2.5 Parameter Estimation

The performance of behavioral PA models and DPD systems depends strongly on accurate estimation of the model coefficients. Several estimation techniques exist, including least-squares (LS), recursive least-squares (RLS), and adaptive gradient-based methods. Among these, least-squares estimation is one of the most commonly used approaches due to its simplicity, computational efficiency, and well-established theoretical properties [9], [22].

2.5.1 PA Model Estimation

Behavioral PA models are typically identified using measured input–output signal pairs. Let $\mathbf{x}$ denote an $N \times 1$ complex input vector applied to the PA, and let $\mathbf{y}$ denote the corresponding measured output vector [9], [22].

For the GMP model, the basis functions are constructed according to (2.10). The resulting regression matrix X contains terms of the form

$$x[n-m]|x[n-m]|^{k-1}, \tag{2.14}$$

$$x[n-m]|x[n-m-l]|^{k-1}, \tag{2.15}$$

and

$$x[n-m]|x[n-m+l]|^{k-1}, \tag{2.16}$$

which correspond to the main polynomial branch, lagging cross terms, and leading cross terms, respectively [6].

Collecting all model coefficients into a parameter vector $\mathbf{w}$, the PA output can be expressed in matrix form as

$$\mathbf{y} = X\mathbf{w}. \tag{2.17}$$

The coefficient vector is then estimated using least-squares regression according to

$$\mathbf{w} = (X^H X)^{-1} X^H \mathbf{y}, \tag{2.18}$$

where X^H denotes the Hermitian transpose of X [22].

In practice, the regression matrix may become ill-conditioned due to highly correlated basis functions. To improve numerical stability and reduce overfitting, regularized least-squares estimation is often used [23], [24],

$$\mathbf{w} = (X^H X + \lambda I)^{-1} X^H \mathbf{y}, \tag{2.19}$$

where λ is a regularization parameter and I denotes the identity matrix. This approach corresponds to ridge regression, also known as Tikhonov regularization [24], [25].

Once the coefficients have been estimated, the modeled PA output is obtained as

$$\hat{\mathbf{y}} = X\mathbf{w}, \tag{2.20}$$

where $\hat{\mathbf{y}}$ denotes the estimated amplifier output signal.

2.5.2 DPD Coefficient Estimation

The estimation of DPD coefficients follows a similar procedure, but instead attempts to reconstruct the PA input from the measured PA output. In this case, the predistorter approximates the inverse behavior of the amplifier [8], [21].

A regression matrix Y is constructed from the measured PA output signal using GMP basis functions. The coefficient vector is then estimated according to

$$\mathbf{w} = (Y^H Y)^{-1} Y^H \mathbf{x}, \tag{2.21}$$

where $\mathbf{x}$ denotes the desired PA input signal.

The estimated predistorted signal is subsequently obtained as

$$\hat{\mathbf{x}} = Y\mathbf{w}. \tag{2.22}$$

The resulting model estimates the PA input from the PA output and therefore behaves as a post-distorter rather than a true predistorter. However, under the assumption that the PA is sufficiently invertible, the estimated post-distorter can be used as a predistorter [8], [21].

2.5.3 Indirect Learning Architecture

The indirect learning architecture (ILA) was first introduced for Volterra predistortion and has since become a common approach for estimating DPD coefficients [8], [21]. In the ILA approach, a post-distorter is first identified using measured PA input–output data. The estimated post-distorter coefficients are then copied directly to the predistorter placed before the PA.

The ILA approach avoids the need for direct optimization of the predistorter inside the transmitter loop and significantly simplifies the coefficient estimation procedure. Due to its simplicity and robustness, ILA has become one of the most widely used learning architectures for digital predistortion systems [8], [9].

2.6 Performance Metrics

To evaluate the performance of the communication system, four complementary metrics are considered: PAPR, NMSE, EVM, and ACLR. Together, these metrics provide insight into the dynamic range, waveform accuracy, modulation quality, and spectral characteristics of the transmitted signal [9], [14].

2.6.1 PAPR

PAPR is used to quantify the dynamic range of a transmitted signal. It describes the relationship between the maximum instantaneous signal power and the average signal power. PAPR is particularly important for multicarrier waveforms such as OFDM, where the superposition of many subcarriers can result in large instantaneous signal peaks [13], [26]. For a discrete-time complex baseband signal $S[n]$, the PAPR in dB is defined as

$$\mathrm{PAPR_{dB}} = 10\log_{10}\left(\frac{\max_n\left(|S[n]|^2\right)}{\frac{1}{N}\sum_{n=1}^{N}|S[n]|^2}\right). \tag{2.23}$$

where $|S[n]|^2$ represents the instantaneous signal power and N is the length of the complex baseband signal.

A high PAPR means that the signal contains large instantaneous peaks compared to its average power. These peaks place stricter requirements on the linearity and dynamic range of the transmitter hardware, especially the power amplifier [1], [2].

If a high-PAPR signal is amplified close to the saturation region of the power amplifier, the peaks may be clipped or compressed. This introduces nonlinear distortion, which can degrade the in-band signal quality and increase out-of-band emissions. As a result, PAPR is closely related to metrics such as EVM, NMSE, and ACLR [1], [14].

To avoid nonlinear distortion, the power amplifier is often operated with input or output back-off, meaning that the average signal power is reduced relative to the saturation power. While this improves linearity, it also lowers the power efficiency of the transmitter. Therefore, a lower PAPR is generally desirable, as it allows the signal to be transmitted more efficiently while maintaining acceptable signal quality and spectral characteristics [1], [2].

2.6.2 EVM

EVM is a commonly used metric for quantifying modulation quality in digital communication systems and is widely used in wireless transmitter conformance testing [14]. It measures how far a received constellation symbol deviates from its ideal reference position in the complex plane, known as the constellation diagram. The deviation is caused by impairments such as noise, nonlinear distortion, phase noise, synchronization errors, and hardware imperfections [9].

For a single transmitted symbol, the error vector is defined as the difference between the ideal transmitted symbol and the corresponding received symbol,

$$e = s_{\mathrm{tx}} - s_{\mathrm{rx}}, \tag{2.24}$$

where s_{tx} denotes the ideal transmitted symbol and s_{rx} denotes the received symbol. The magnitude of this vector, $|e|$, represents the instantaneous error for that symbol.

In practice, EVM is evaluated over a sequence of N received symbols. The most commonly used measure is the RMS EVM, which provides an average measure of the modulation error across all symbols. Assuming that the reference constellation is normalized to unit average power, the RMS EVM, expressed as a percentage, is given by

$$\mathrm{EVM}_{\mathrm{RMS}} = 100\sqrt{\frac{1}{N}\sum_{k=1}^{N} |s_{\mathrm{tx},k} - s_{\mathrm{rx},k}|^2}. \tag{2.25}$$

A lower RMS EVM indicates that the received symbols are located closer to their ideal constellation points, corresponding to higher modulation accuracy and improved signal quality [14].

In addition to the RMS value, the maximum EVM is often reported to characterize the worst-case symbol error within the measured sequence. It is defined as

$$\mathrm{EVM}_{\mathrm{max}} = 100 \max_{k} \left(|s_{\mathrm{tx},k} - s_{\mathrm{rx},k}| \right). \tag{2.26}$$

While RMS EVM reflects the average modulation accuracy, the maximum EVM highlights the largest instantaneous deviation observed during the measurement interval.

2.6.3 ACLR

ACLR is a metric used to quantify out-of-band emissions in wireless communication systems. It describes how much signal power leaks from the intended transmission channel into adjacent frequency channels due to impairments such as nonlinear distortion, spectral regrowth, and hardware imperfections [9], [14].

ACLR is defined as the ratio of adjacent-channel power to main-channel power,

$$\mathrm{ACLR} = \frac{P_{\mathrm{adj}}}{P_{\mathrm{ch}}}, \tag{2.27}$$

where P_{ch} is the power contained in the main transmission channel and P_{adj} is the power measured in the adjacent channel.

Since the adjacent channel power is typically much smaller than the in-band channel power, ACLR is commonly expressed in decibels (dB),

$$\mathrm{ACLR}_{\mathrm{dB}} = 10 \log_{10} \left(\frac{P_{\mathrm{adj}}}{P_{\mathrm{ch}}} \right). \tag{2.28}$$

A more negative ACLR corresponds to lower spectral leakage and therefore improved spectral confinement of the transmitted signal.

The exact definition of ACLR depends on the communication standard and measurement setup, including the channel bandwidth, measurement filter, and channel spacing [14]. In this thesis, ACLR is evaluated separately for the lower and upper adjacent channels, using the ratio of adjacent-channel power to main-channel power. The adjacent channels are assumed to be located directly next to the main channel without any additional guard band or channel spacing.

2.6.4 NMSE

NMSE is used to quantify the overall distortion between transmitted and received complex baseband signals. Unlike EVM, which evaluates symbol-wise constellation errors, NMSE measures the discrepancy between the complete transmitted and received signal waveforms and is commonly used when evaluating behavioral PA models and DPD performance [5], [6], [27].

Prior to the NMSE calculation, the transmitted and received signals are synchronized in frequency, phase, and time. In addition, the received signal is scaled such that both signals have equal average power. This ensures that the NMSE reflects waveform distortion rather than differences in signal amplitude [9].

The NMSE is defined as

$$\mathrm{NMSE} = \frac{\sum_n |S_{\mathrm{tx}}[n] - S_{\mathrm{rx}}[n]|^2}{\sum_n |S_{\mathrm{tx}}[n]|^2}, \tag{2.29}$$

where $S_{\mathrm{tx}}[n]$ and $S_{\mathrm{rx}}[n]$ denote the transmitted and received complex baseband samples, respectively.

The numerator represents the total error power between the transmitted and received signals, while the denominator normalizes the error with respect to the transmitted signal power. A lower NMSE therefore indicates a more accurate reconstruction of the transmitted waveform and improved overall system performance.

NMSE is often expressed in decibels (dB) according to

$$\mathrm{NMSE}_{\mathrm{dB}} = 10 \log_{10}(\mathrm{NMSE}). \tag{2.30}$$

3
Methods

This project began with the implementation of several digital communication links in MATLAB. Two single-carrier QAM waveforms and two OFDM waveforms were evaluated. The baseline performance of the communication systems was assessed using standard metrics including EVM, ACLR, and NMSE.

Subsequently, behavioral PA models were introduced in order to emulate nonlinear distortion effects. DPD models were then trained and evaluated for different waveform and PA combinations. Finally, additional studies investigating model complexity, robustness to noise, and PA mismatch were conducted.

3.1 Communication System Implementation

There are several modulation formats used in communication systems. In this thesis, two single-carrier modulated signals were used as well as two OFDM signals.

3.1.1 Single-Carrier Waveforms

Two single-carrier modulation formats were implemented: QPSK and 16-QAM. The transmitter chain is illustrated in Fig. 3.1.

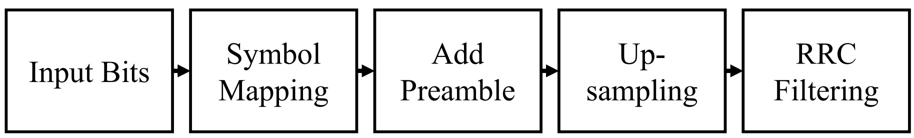

Figure 3.1: Block diagram of the single-carrier transmitter chain.

First, 1×10^4 random bits were generated using MATLAB's default random number generator. The bits were then mapped onto normalized Gray-coded QAM constellations. A repeated 13-bit BPSK-modulated Barker sequence was appended to the beginning of the frame to serve as a synchronization preamble for frame synchronization and carrier recovery.

The resulting symbol stream was upsampled by a factor of 10 (SPS = 10) and pulse-shaped using a root-raised cosine (RRC) filter with a roll-off factor of $\beta = 0.2$ and a filter span of 10 symbols (span = 10).

After transmission, several channel impairments were introduced to emulate realistic communication conditions. These impairments included random carrier frequency offset (CFO), random phase offset, and random timing offset. Optional additive white Gaussian noise (AWGN) was also included to simulate noisy channel conditions.

The impaired signal was subsequently processed by the receiver chain shown in Fig. 3.2. Frame synchronization was performed by correlating the received signal with a locally generated version of the preamble, which had undergone the same upsampling and filtering operations as in the transmitter. Once the frame start was detected, the total filter delay,

$$2 \times \frac{\text{span} \times \text{SPS}}{2},$$

was removed.

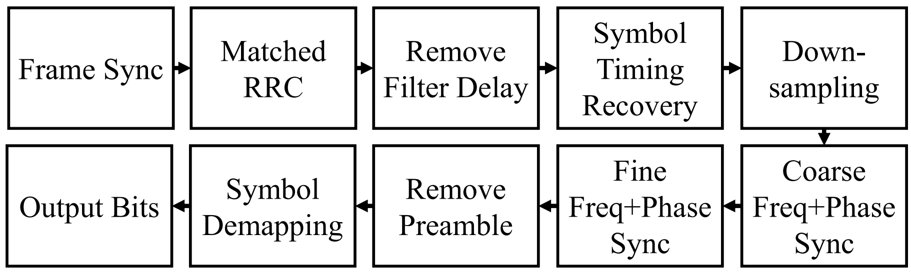

Figure 3.2: Block diagram of the single-carrier receiver chain.

The frequency correction first used the known preamble to estimate and remove the main carrier frequency and phase offset. After stripping off the known preamble symbols, the remaining phase rotation was fit with a straight line; its slope gave the coarse frequency offset and its intercept gave the phase offset. This correction was applied to the full frame. A finer tracking loop then removed residual error: it used the known preamble for reliable updates, then switched to decision-directed tracking on the payload, updating only when symbol decisions were confident. The result was a stabilized received signal with reduced carrier rotation and drift.

3.1.2 OFDM Waveforms

Two OFDM-based waveforms were considered: one conventional CP-OFDM and one DFT-s-OFDM. The implemented transmitter chain corresponds to the DFT-s-OFDM case, while CP-OFDM is obtained by omitting the DFT spreading and inverse spreading operations.

The payload bit stream was generated and mapped in the same manner as for the single-carrier systems. Random bits were grouped and mapped to normalized 16-QAM constellation symbols. The mapped symbols were then reshaped into blocks of $N_{sc} = 50$ symbols, where each block corresponds to one DFT-s-OFDM symbol.

A total of 50 payload blocks were used.

In contrast to the single-carrier implementation, no pulse shaping or explicit symbol-rate upsampling was applied. Instead, each block of N_{sc} QAM symbols was processed by the multicarrier modulation chain. For DFT-s-OFDM, an N_{sc}-point DFT was first applied to the QAM-symbol block. The resulting frequency-domain samples were then mapped to a localized set of active subcarriers in an $N_{\text{fft}} = 200$-point frequency grid. The allocation was centred around DC while excluding the DC subcarrier, with $N_{sc}/2$ subcarriers placed below DC and $N_{sc}/2$ placed above DC. For CP-OFDM, the same localized subcarrier allocation is used, but the DFT spreading stage is omitted.

After subcarrier mapping, an N_{fft}-point IFFT was used to generate the time-domain OFDM symbol. Each symbol was extended by a cyclic prefix of length $N_{cp} = 16$. In addition, weighted overlap-and-add (WOLA) windowing was applied using an overlap length $N_{\text{wola}} = 8$. This was implemented by adding a cyclic suffix of length N_{wola}, applying complementary raised-cosine fade-in and fade-out windows to the beginning and end of each extended symbol, and overlap-adding adjacent symbols with a hop size of $N_{\text{fft}} + N_{cp}$. Setting $N_{\text{wola}} = 0$ reduces the processing to standard cyclic-prefix insertion without WOLA.

A known synchronization preamble was prepended to the payload. The preamble was generated from $2N_{sc}$ random bits using a fixed random seed and QPSK modulation. The resulting N_{sc} QPSK symbols were DFT-spread, mapped to the same localized active subcarriers, and transformed to the time domain using the same IFFT operation as the payload. Two identical preamble symbols were then transmitted consecutively and processed using the same WOLA overlap-add procedure. The repeated preamble structure was used for frame synchronization and coarse CFO estimation.

The transmitter structure for the DFT-s-OFDM waveform is shown in Fig. 3.3. The main structural difference between CP-OFDM and DFT-s-OFDM is the inclusion of the DFT spreading stage before subcarrier mapping and the corresponding inverse DFT stage at the receiver. Due to this spreading operation, each data symbol in DFT-s-OFDM is distributed over all allocated subcarriers, which generally reduces the PAPR compared with conventional CP-OFDM.

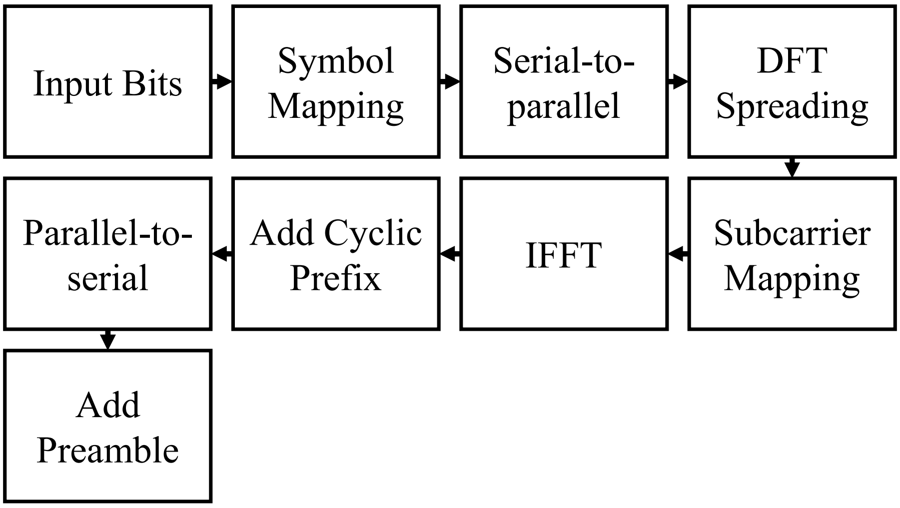

Figure 3.3: Block diagram of the discrete Fourier transform spread orthogonal frequency division multiplexing transmitter chain.

The transmitted signal was passed through the same impairment model as the single-carrier systems. The channel model applied a random timing offset, a random phase offset, and a normalized frequency offset. AWGN was also added according to the selected SNR value.

At the receiver, frame synchronization was performed by correlating the received signal with the known WOLA-processed preamble sequence. The start of the frame was estimated from the peak of this correlation metric. Coarse CFO estimation was then performed using the two repeated preamble symbols. Specifically, the useful N_{fft}-sample portions of the two preamble blocks were compared, and the phase difference over one WOLA symbol hop was used to estimate the normalized CFO. The estimated CFO was compensated over the full received signal.

After coarse CFO correction, a common phase offset was estimated using the full known preamble and removed from the received signal. The payload portion was then extracted using the known preamble length and the OFDM/WOLA block spacing. A residual CFO estimate was additionally obtained from the cyclic prefix of each payload block. To avoid the samples affected by WOLA overlap, the first N_{wola} samples of the cyclic prefix were excluded from this estimate. The final fine CFO estimate was computed as the average of the per-block estimates and was applied to the extracted data portion.

The DFT-s-OFDM demodulation then proceeded block-wise. For each received data block, the FFT window was placed after the cyclic prefix, and an N_{fft}-point FFT was applied. The localized active subcarriers were then extracted from the FFT-shifted frequency grid. For DFT-s-OFDM, an N_{sc}-point inverse DFT was applied to recover the QAM-symbol estimates. For CP-OFDM, this inverse spreading step is omitted.

Finally, a decision-directed common phase correction was applied independently to each received symbol block. Each estimated symbol was first mapped to its nearest reference constellation point, and the resulting block-wise phase error was estimated and compensated. The corrected QAM symbols were then serialized, normalized by their RMS value, and demapped to output bits. The receiver structure is shown in Fig. 3.4.

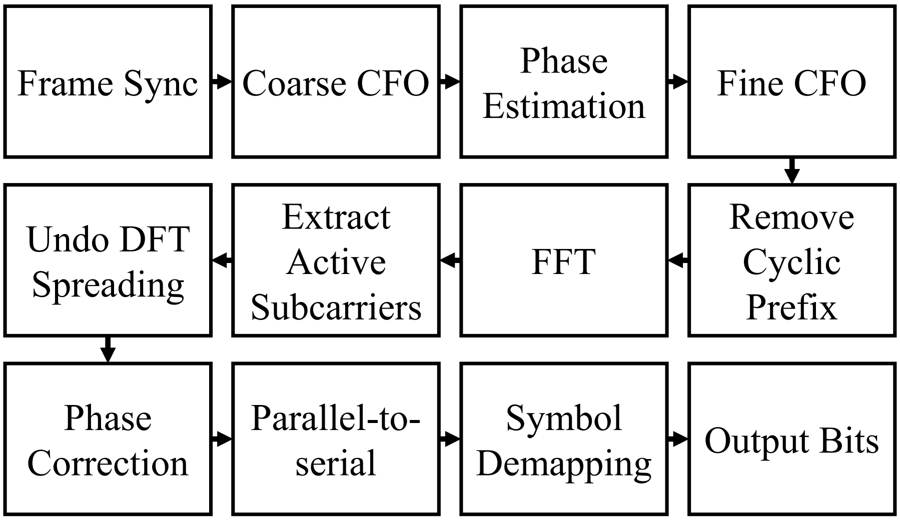

Figure 3.4: Block diagram of the discrete Fourier transform spread orthogonal frequency division multiplexing receiver chain.

3.2 GMP Model Simplifications

To reduce the model complexity for both the PA model and the DPD models, the GMP structure in (2.10) was simplified by setting

$$K_a = K_b = K_c = K,$$

$$M_a = M_b = M_c = M,$$

and

$$L_b = L_c = L.$$

This simplified the parameter optimization process while still preserving the dominant nonlinear memory effects. However, when minimizing the total number of coefficients, these parameters may be independently optimized.

Furthermore, only odd-order polynomial terms were included in both the GMP PA and DPD models, as they dominate the in-band intermodulation distortion and spectral regrowth generated by RF power amplifiers. Even-order terms generally contribute less to the distortion of interest and have been shown not to provide a richer description of PA behavior [28].

Additionally, the lagging and leading cross terms were included starting from third order. For $k = 1$, the cross terms reduce to $x[n-m]|x[n-m\pm l]|^0 = x[n-m]$, which is already included in the main branch. Hence, these terms add redundant basis functions without increasing the modeling capability, while increasing the number of estimated parameters. The resulting simplified GMP model is given in (3.1).

$$
\begin{aligned}
y[n] = & \sum_{\substack{k=1\\ k \text{ odd}}}^{K} \sum_{m=0}^{M} a(k,m) x[n-m] |x[n-m]|^{k-1} \\
& + \sum_{\substack{k=3\\ k \text{ odd}}}^{K} \sum_{m=0}^{M} \sum_{l=1}^{L} b(k,m,l) x[n-m] |x[n-m-l]|^{k-1} \\
& + \sum_{\substack{k=3\\ k \text{ odd}}}^{K} \sum_{m=0}^{M} \sum_{l=1}^{L} c(k,m,l) x[n-m] |x[n-m+l]|^{k-1}.
\end{aligned}
\tag{3.1}
$$

3.3 Power Amplifier Modeling

Behavioral power amplifier models were introduced in order to emulate nonlinear distortion effects commonly observed in practical RF transmitters. Two different PA models were considered: a memoryless Saleh model representing a TWTA, and a GMP model representing a SSPA.

3.3.1 TWTA Saleh Model

The TWTA was modeled using the memoryless Saleh model described in [3]. The model parameters were extracted from measurements of a real TWTA [3] and are summarized in Table 3.1.

Table 3.1: Saleh parameters used to emulate a realistic TWTA.

α_a	1.6623
α_ϕ	0.1533
β_a	0.0552
β_ϕ	0.3456

The Saleh model was selected due to its ability to accurately capture both AM/AM and AM/PM nonlinear characteristics commonly observed in traveling-wave tube amplifiers.

3.3.2 SSPA GMP Model

The SSPA was modeled using the simplified GMP model given in (3.1). The GMP coefficients were identified by solving the regularized least-squares problem in (2.19), using $\lambda = 1 \times 10^{-6}$. The identification was performed using the `APA_200MHz` dataset from OpenDPD/OpenDPDv2 [27], [29]. This dataset contains measured complex baseband input–output samples from a TM3.1a 200 MHz OFDM test signal transmitted through a real 3.5 GHz GaN Doherty power amplifier.

The measured output signal therefore captures the nonlinear amplitude, phase, and memory effects introduced by the hardware PA. After coefficient extraction, the resulting GMP parameters were used to implement the behavioral SSPA model according to (2.20).

3.3.3 PA Model Validation

To achieve a close approximation of the measured PA characteristics, a maximum polynomial order of 5, a memory depth of 3, and 2 lagging/leading cross terms were selected.

Using this configuration, the GMP model achieved an NMSE of -31.21 dB between the measured PA output and the modeled output signal.

The resulting AM/AM and AM/PM characteristics of both PA models are shown in Fig. 3.5.

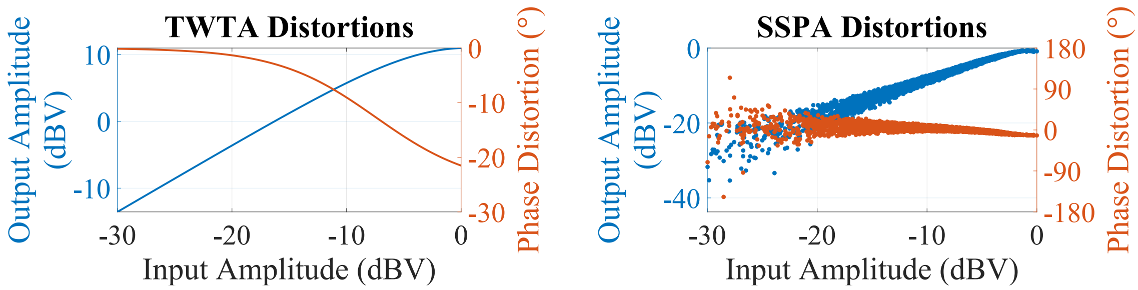

(a) TWTA **(b)** SSPA

Figure 3.5: Input versus output characteristics of the TWTA and SSPA.

3.4 Digital Predistortion Modeling

The DPD models were evaluated in several stages. First, a baseline evaluation of the communication links was conducted without any PA distortion in order to establish reference performance levels.

Next, the two PA models were inserted directly after the transmitter chain to evaluate the nonlinear distortion introduced by each amplifier model for all considered waveforms.

Finally, DPD models were trained and applied to compensate for the PA nonlinearities. For the parameter extraction process, both the PA input and PA output signals were stored and used within the DPD parameter estimator.

For the TWTA case, a memoryless polynomial DPD model with odd polynomial orders up to ninth order was employed. For the SSPA case, a GMP-based DPD model was used. A summary of the DPD model configurations is provided in Table 3.2.

Table 3.2: A summary of the number of parameters used for each of the DPD models.

Model	TWTA DPD	SSPA DPD
Max Polynomial Order	9	7
Max Memory Depth	0	5
Max lagging/leading terms	0	3
Total number of parameters	5	132

3.5 Complexity Reduction Study

After establishing the baseline DPD performance, a complexity reduction study was performed. In this part, the complexity of each model was reduced and swept over the different parameters.

The performance of the DPD model is presented against the complexity of the model. First, the polynomial model is tested with different maximum polynomial orders against the Saleh model given in (2.3). For this test, the NMSE, ACLR, and EVM are evaluated.

After the memoryless DPD is evaluated against the TWTA model, the GMP model is evaluated with different maximum polynomial orders, maximum memory depths, and maximum lagging/leading terms.

A summary of the maximum DPD model configurations is provided in Table 3.3.

Table 3.3: A summary of the maximum number of parameters used for each of the DPD models when performing the parameter sweep.

Model	TWTA DPD	SSPA DPD
Max Polynomial Order	15	7
Max Memory Depth	0	6
Max lagging/leading terms	0	6
Total number of parameters	8	280

3.6 Noise Robustness Analysis

The models were then tested against noise. First, input noise was tested where the DPD parameters were extracted from an ideal input and output. The parameters were then frozen. AWGN was then applied to the input of the power amplifier with signal-to-noise ratios between 25 dB and 50 dB with steps of 5 dB. The DPD was then applied with the frozen parameters extracted from the ideal PA input and output, followed by the PA model. Finally, the performance of each PA and DPD model was evaluated. Since the noise was applied to the signal itself, rendering the calculations for ACLR and NMSE invalid, only the EVM was calculated for this test.

Moreover, the models were also tested against output training noise (AWGN), where the SNR was swept between 15 dB and 50 dB with steps of 5 dB. In this test, the noise was applied to the output of the power amplifier before extracting the DPD parameters. Thus, the parameters were extracted from a noisy output signal. The DPD was then applied to an ideal signal using these parameters. EVM, ACLR, and NMSE were then calculated.

3.7 Power Amplifier Mismatch

To evaluate whether the DPD would still work with a slightly different power amplifier, a power amplifier mismatch test was conducted. First, the DPD parameters were extracted in the ideal case and applied to the respective signal. Then, different parts of the power amplifier model were changed.

For the TWTA model, the linear gain was first varied by ± 1 dB, followed by varying the input level at which the signal entered compression by $\pm 5\%$. The amplitude-to-phase distortion was then varied by $\pm 5\%$. Finally, random impairments were introduced by multiplying the four parameters by noise levels of 2% and 5%. To obtain reliable results, the tests involving random impairments were repeated 100 times, and the mean value of each performance metric was computed.

The tests for the SSPA mismatch were similar to those for the TWTA mismatch. First, the linear gain was varied by ± 1 dB, followed by varying the linear memory drift by ± 1 dB. Static nonlinear drift, nonlinear memory drift, and nonlinear lagging/leading drift were then introduced, each varied by $\pm 5\%$. A nonlinear phase shift was subsequently applied by changing the phase of the GMP parameters by $\pm 3^\circ$. Finally, random impairments were introduced in the same manner as for the TWTA model mismatch, where 2% and 5% complex white noise were added to each parameter. These tests were repeated 100 times, and the average performance was computed.

4
Results and Discussion

In this chapter, the results of the thesis are presented and discussed. First, a baseline performance is established, followed by the complexity reduction study. Then, a noise analysis and a power amplifier mismatch analysis are performed. Finally, future work and limitations of the thesis are discussed.

4.1 Baseline performance

This section presents the baseline performance of the implemented communication link. The evaluation includes three cases: the undistorted reference link, the performance degradation introduced by the nonlinear PA models, and the performance obtained when DPD is applied together with the PA models.

4.1.1 Optimal scenario

The baseline performance of the implemented communication links under ideal operating conditions is presented in Tab. 4.1. In this scenario, neither power amplifier distortion nor additive noise is applied. The results therefore represent the intrinsic performance limitations of the implemented transmitter and receiver chains.

Table 4.1: Baseline performance metrics of the different signals used.

Modulation	PAPR (dB)	Lower ACLR (dB)	Upper ACLR (dB)	NMSE (dB)	$\mathrm{EVM}_{\mathrm{RMS}}$ (%)
QPSK	5.20	-38.49	-38.07	$-\infty$	0.73
16-QAM	6.79	-37.57	-36.64	$-\infty$	0.71
DFT-s-OFDM	8.03	-25.23	-26.19	$-\infty$	0.00
CP-OFDM	8.85	-26.24	-25.56	$-\infty$	0.00

As expected, the OFDM-based waveforms exhibit the highest PAPR, with CP-OFDM reaching the largest value of 8.85 dB. The DFT-s-OFDM waveform achieves a slightly lower PAPR due to the DFT-spreading operation, which distributes the symbol energy more evenly across the allocated subcarriers. In contrast, the single-carrier waveforms exhibit lower PAPR values, particularly the QPSK signal.

The ACLR results also reflect the different spectral characteristics of the evaluated waveforms. The single-carrier signals achieve significantly lower adjacent-channel leakage compared to the OFDM-based signals, primarily due to the root-raised cosine filtering used in the transmitter chain.

The NMSE is equal to $-\infty$ dB for all waveforms, since the transmitted and received signals are identical after synchronization and normalization in the ideal case. Furthermore, the OFDM-based waveforms achieve nearly zero EVM, while the single-carrier signals exhibit slightly higher EVM values. These small residual errors are mainly attributed to synchronization inaccuracies and imperfections introduced by the pulse-shaping and matched-filtering operations.

The single-carrier constellation diagram for the ideal 16-QAM scenario is presented in Fig. 4.1.

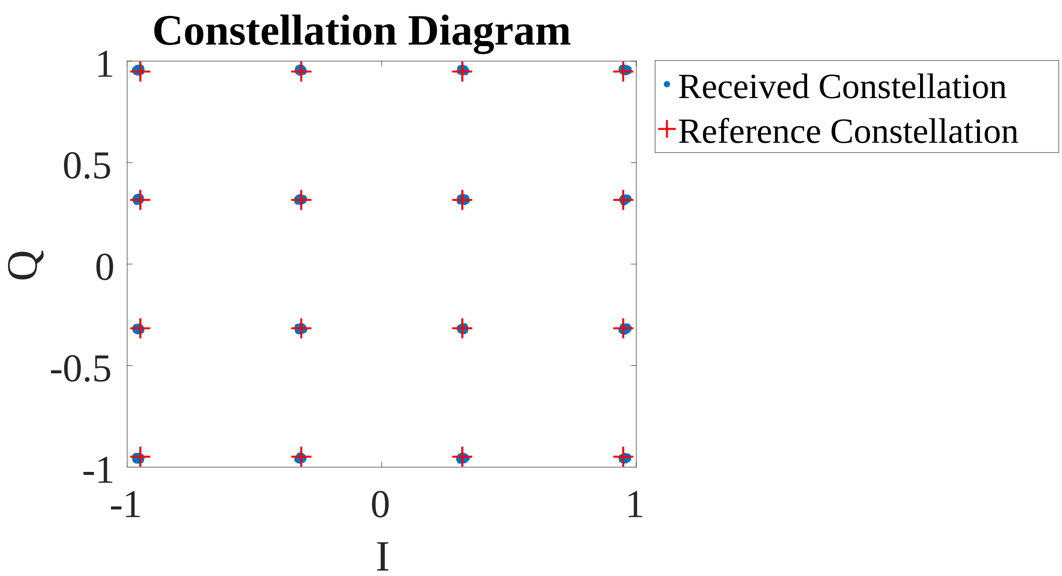

Figure 4.1: Single-carrier constellation diagram of the 16-QAM signal with 2500 symbols, 10 samples per symbol, a roll-off $\beta = 0.2$, and a span of 10.

As shown in Fig. 4.1, the received constellation points are tightly clustered around the ideal reference symbols. This indicates that the implemented transmitter and receiver chains operate correctly under ideal conditions. Only minor deviations from the ideal constellation locations are observed.

The constellation also maintains a clear separation between all symbol points, resulting in zero bit errors for the evaluated frame. The small symbol spread is consistent with the low EVM values reported in Tab. 4.1. This figure therefore serves as a useful reference for later comparisons, where the effects of PA nonlinearities and the performance of the DPD models are evaluated.

4.1.2 PA distortion

In this section, the effects of the two implemented PA models on the different communication signals are evaluated. First, the distortions introduced by the memoryless

TWTA model are analyzed. The GMP SSPA model is then evaluated. The resulting degradation in constellation quality, spectral containment, and overall signal quality is quantified using the previously defined performance metrics.

4.1.2.1 TWTA

The baseline performance metrics of the communication signals after distortion by the TWTA model are presented in Tab. 4.2.

Table 4.2: Baseline performance metrics of the traveling-wave tube amplifier with the evaluated signals.

Modulation	Lower ACLR (dB)	Upper ACLR (dB)	NMSE (dB)	$\mathrm{EVM_{RMS}}$ (%)
QPSK	-26.06	-25.89	-10.42	5.49
16-QAM	-25.73	-25.70	-10.91	8.95
DFT-s-OFDM	-21.63	-21.75	-11.57	9.10
CP-OFDM	-22.08	-21.64	-11.64	10.72

As shown in Tab. 4.2, the TWTA model significantly degrades the performance of all evaluated waveforms. The ACLR values are substantially worse than in the ideal case, indicating pronounced spectral regrowth caused by the nonlinear compression characteristics of the amplifier. This degradation is particularly noticeable for the OFDM-based waveforms, which show the poorest ACLR performance due to their inherently high PAPR.

The EVM values also increase considerably for all waveforms, demonstrating the negative impact of the TWTA nonlinearities on constellation quality. The CP-OFDM waveform experiences the largest degradation, reaching an EVM of 10.72%. This is consistent with its high PAPR and increased sensitivity to static nonlinear distortion. In comparison, the QPSK signal achieves the lowest EVM, which can be attributed to its lower envelope variations and reduced susceptibility to compression effects.

The resulting constellation distortion of the 16-QAM signal after TWTA amplification is illustrated in Fig. 4.2.

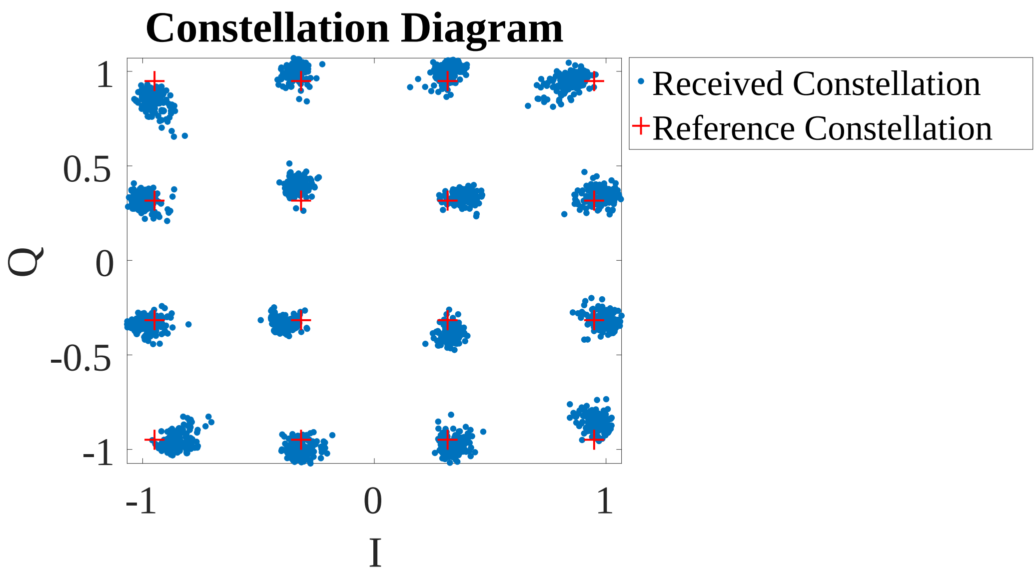

Figure 4.2: Single-carrier constellation diagram of the 16-QAM signal with 2500 symbols, 10 samples per symbol, a roll-off $\beta = 0.2$, and a span of 10. The signal is distorted using the TWTA model.

As shown in Fig. 4.2, the constellation points are no longer tightly clustered around the ideal symbol locations. Instead, both radial spreading and angular rotation are observed, corresponding to the AM/AM and AM/PM distortions introduced by the TWTA model. The outer constellation points are affected most severely, since these symbols have higher instantaneous amplitudes and are therefore driven further into the nonlinear compression region of the amplifier.

Despite the increased symbol dispersion, the constellation clusters remain sufficiently separated for most symbols to be detected correctly. However, the reduced decision margins increase the sensitivity to additional impairments, such as additive noise and synchronization errors. Fig. 4.2 therefore clearly demonstrates the need for digital predistortion to compensate for the nonlinear TWTA behavior and restore the constellation quality.

4.1.2.2 SSPA

The constellation diagram illustrating the distortion introduced by the SSPA model is shown in Fig. 4.3.

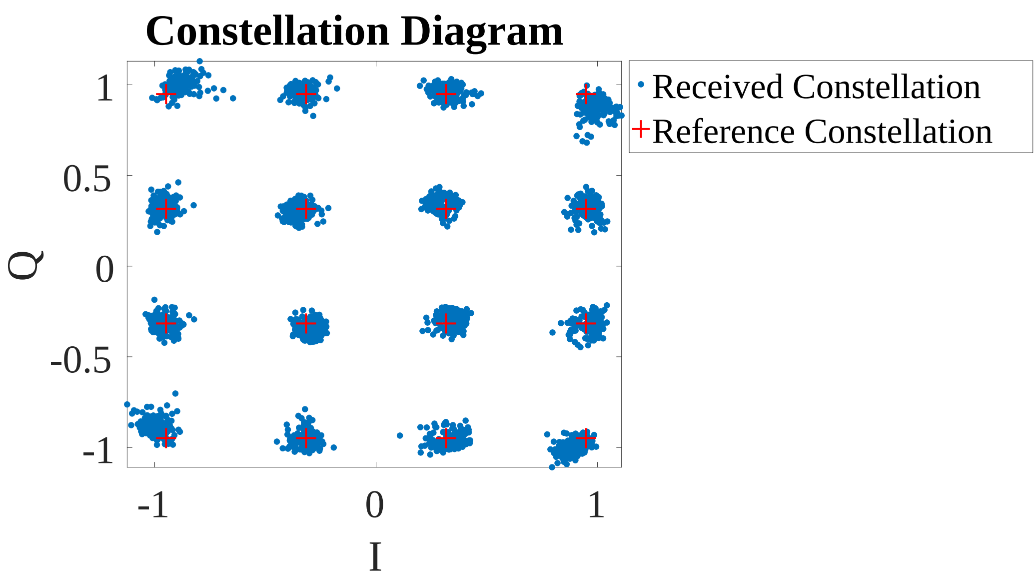

Figure 4.3: Single-carrier constellation diagram of the 16-QAM signal with 2500 symbols, 10 samples per symbol, a roll-off $\beta = 0.2$, and a span of 10. The signal is distorted using the GMP-based SSPA model.

As shown in Fig. 4.3, the SSPA model introduces substantial constellation spreading and distortion. Compared to the TWTA case, the distortion pattern appears less symmetric, which is consistent with the memory effects included in the GMP-based amplifier model. The constellation points exhibit both amplitude compression and phase distortion, causing the received symbols to deviate from their ideal locations.

The outer constellation points are again affected more severely due to their higher instantaneous amplitudes. However, in contrast to the memoryless TWTA model, the SSPA model also introduces additional spreading due to memory effects. This results in a less regular constellation deformation and highlights the increased complexity associated with linearizing SSPAs compared to memoryless amplifiers.

The baseline performance metrics for the SSPA distortion case are summarized in Tab. 4.3.

Table 4.3: Baseline performance metrics of the solid-state amplifier model with the evaluated signals.

Modulation	Lower ACLR (dB)	Upper ACLR (dB)	NMSE (dB)	$\mathrm{EVM}_{\mathrm{RMS}}$ (%)
QPSK	-29.75	-29.30	-19.50	6.21
16-QAM	-29.70	-29.02	-20.16	7.67
DFT-s-OFDM	-23.31	-24.96	-18.93	8.78
CP-OFDM	-23.90	-24.22	-18.73	9.48

From Tab. 4.3, it can be observed that the SSPA model introduces considerable degradation for all evaluated waveforms. Similar to the TWTA case, the OFDM-based signals exhibit the worst ACLR performance due to their high PAPR characteristics. However, the ACLR values are slightly improved compared to the TWTA case, indicating that the SSPA model produces less severe spectral regrowth under the evaluated conditions.

The EVM values show that the OFDM-based waveforms remain the most sensitive to nonlinear distortion, with DFT-s-OFDM and CP-OFDM reaching the highest EVM values. The single-carrier waveforms achieve lower EVM values, suggesting that the SSPA memory effects have a stronger impact on multicarrier waveforms than on single-carrier signals.

The NMSE results further indicate that the SSPA-induced distortion is substantial, although generally less severe than the TWTA distortion for the single-carrier cases. However, due to the inclusion of memory effects in the GMP-based amplifier model, the resulting distortion is more waveform-dependent and more difficult to compensate.

4.1.3 DPD baseline performance

In this section, the baseline performance of the implemented digital predistortion models is evaluated for both the TWTA and SSPA amplifier models. The objective is to investigate how effectively the full DPD models compensate for the nonlinear distortions introduced by the amplifiers and restore the communication link performance.

4.1.3.1 TWTA

The power spectral density (PSD) of the single-carrier 16-QAM signal is presented in Fig. 4.4.

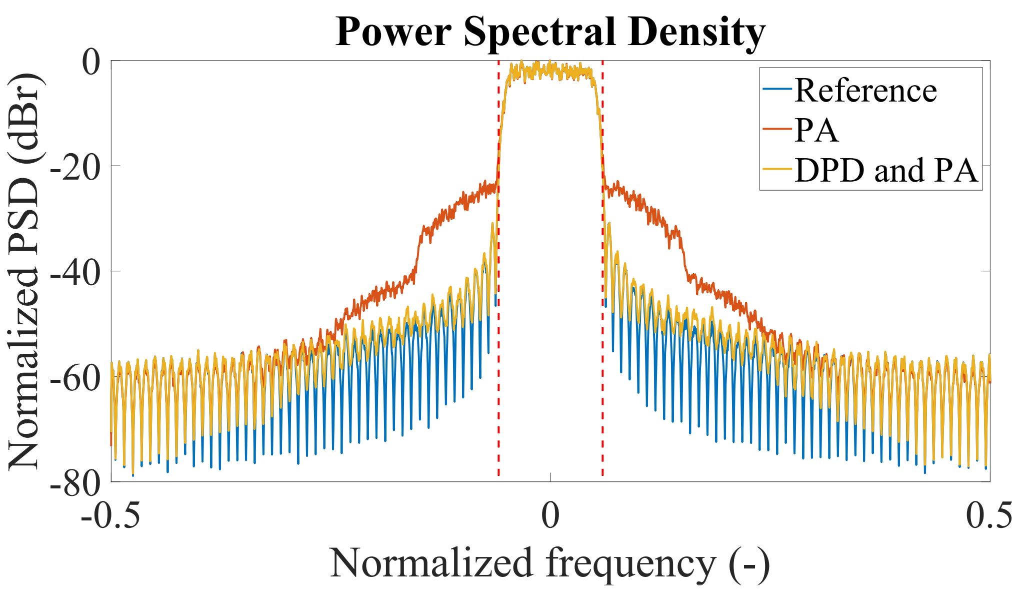

Figure 4.4: Power spectral density of the 16-QAM signal without distortion, with TWTA distortion, and with polynomial DPD followed by the TWTA model. The DPD uses odd-order polynomials up to order 9. Both axes are normalized: the y-axis is normalized relative to the maximum value, and the x-axis is normalized frequency.

As shown in Fig. 4.4, the TWTA model introduces significant spectral regrowth compared to the undistorted reference signal. The nonlinear compression of the amplifier causes signal energy to spread into adjacent frequency bands, resulting in substantial ACLR degradation. When the polynomial DPD model is applied prior to amplification, the spectral regrowth is significantly reduced and the PSD approaches that of the ideal undistorted signal.

The effectiveness of the DPD model can also be observed in the constellation diagram shown in Fig. 4.5.

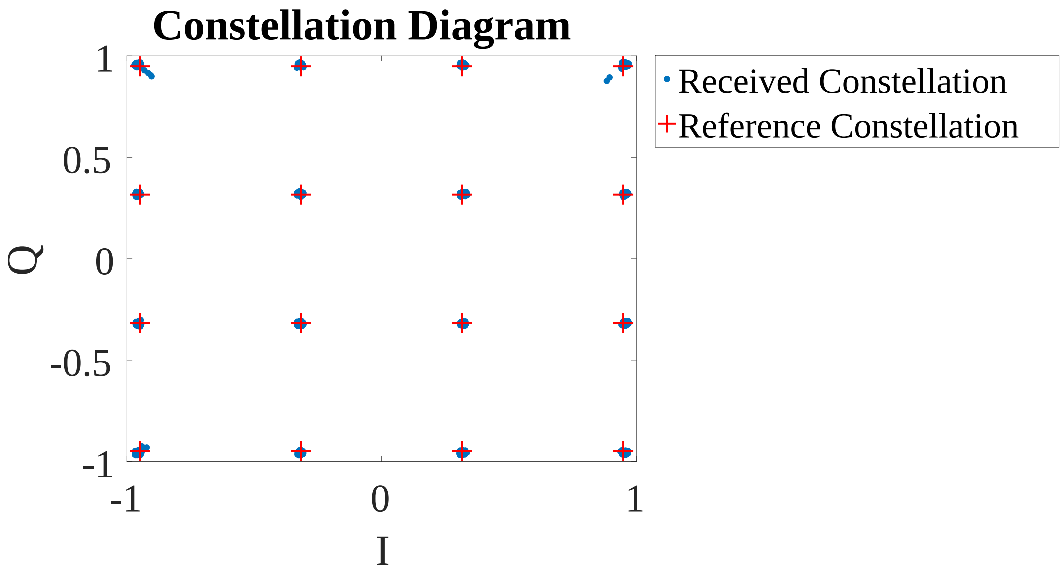

Figure 4.5: Single-carrier constellation diagram of the 16-QAM signal with 2500 symbols, 10 samples per symbol, a roll-off $\beta = 0.2$, and a span of 10. The signal is predistorted using the polynomial DPD model and subsequently amplified using the TWTA model.

Compared to the distorted constellation presented previously, the DPD-compensated constellation points are significantly more concentrated around their ideal symbol locations. The radial spreading and phase rotation introduced by the TWTA are largely removed, demonstrating that the polynomial DPD successfully approximates the inverse characteristics of the amplifier.

A small number of symbols still exhibit minor deviations from their ideal locations, particularly among the outer constellation points where the nonlinear compression is strongest. Nevertheless, the remaining distortion is sufficiently small that all symbols remain within their correct decision regions, resulting in zero bit errors for the evaluated frame.

A summary of the baseline DPD performance for the TWTA model is presented in Tab. 4.4.

Table 4.4: Baseline performance metrics of the polynomial DPD model when cascaded with the TWTA model.

Modulation	Lower ACLR (dB)	Upper ACLR (dB)	NMSE (dB)	EVM_{RMS} (%)
QPSK	-38.28	-37.88	-44.16	0.77
16-QAM	-37.26	-36.40	-41.70	0.85
DFT-s-OFDM	-25.26	-26.19	-39.98	0.52
CP-OFDM	-26.19	-25.53	-39.10	0.72

The results in Tab. 4.4 show that the polynomial DPD model restores the communication performance close to the ideal undistorted case. The ACLR values improve significantly for all waveforms compared to the uncompensated TWTA case, indicating that the spectral regrowth has been effectively suppressed.

The EVM values are also substantially reduced and approach the ideal baseline values. Similarly, the NMSE values improve dramatically for all waveforms, confirming that the predistorter accurately compensates for the TWTA nonlinearities.

Overall, these results demonstrate that a relatively low-complexity memoryless polynomial DPD model is sufficient to effectively linearize the memoryless TWTA amplifier model.

4.1.3.2 SSPA

The power spectral density of the single-carrier 16-QAM signal after SSPA distortion and DPD compensation is presented in Fig. 4.6. In this baseline evaluation, the GMP DPD configuration uses odd-order polynomials up to order 7, a memory depth of 5, and 3 lagging/leading cross terms. This configuration is used as a high-complexity reference before the complexity reduction study in Section 4.2.

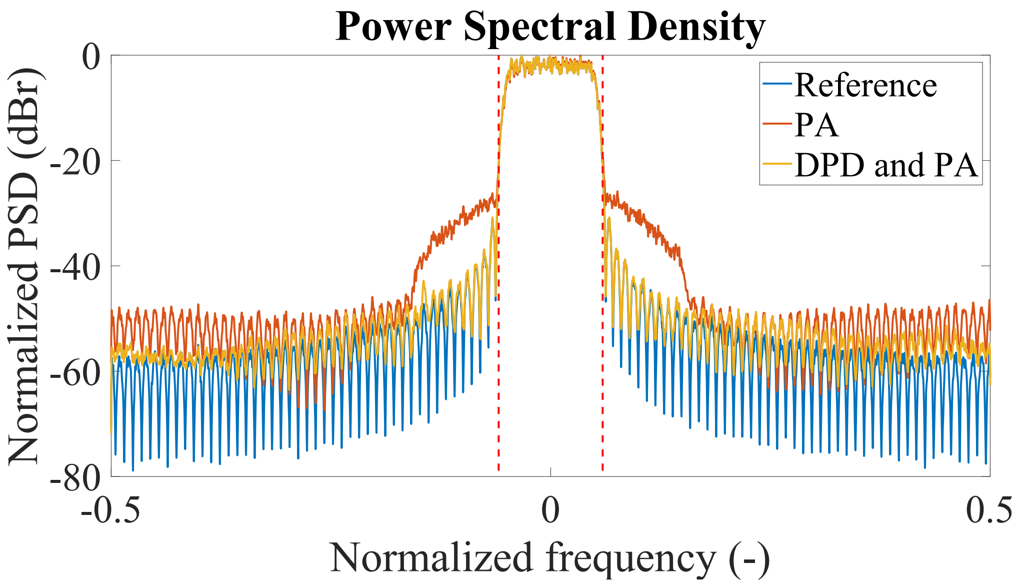

Figure 4.6: Power spectral density of the 16-QAM signal without distortion, with SSPA distortion, and with GMP DPD followed by the SSPA model. The DPD uses odd-order polynomials up to order 7, with memory depth of 5 and 3 lagging/leading cross terms. Both axes are normalized: the y-axis is normalized relative to the maximum value, and the x-axis is normalized frequency.

As shown in Fig. 4.6, the SSPA model introduces substantial spectral regrowth due to its nonlinear and memory-dependent behavior. The adjacent-channel leakage increases significantly compared to the ideal case. However, when the GMP-based DPD model is applied, the spectral regrowth is strongly reduced and the PSD approaches the undistorted reference spectrum.

The corresponding constellation diagram for the DPD-compensated SSPA case is shown in Fig. 4.7.

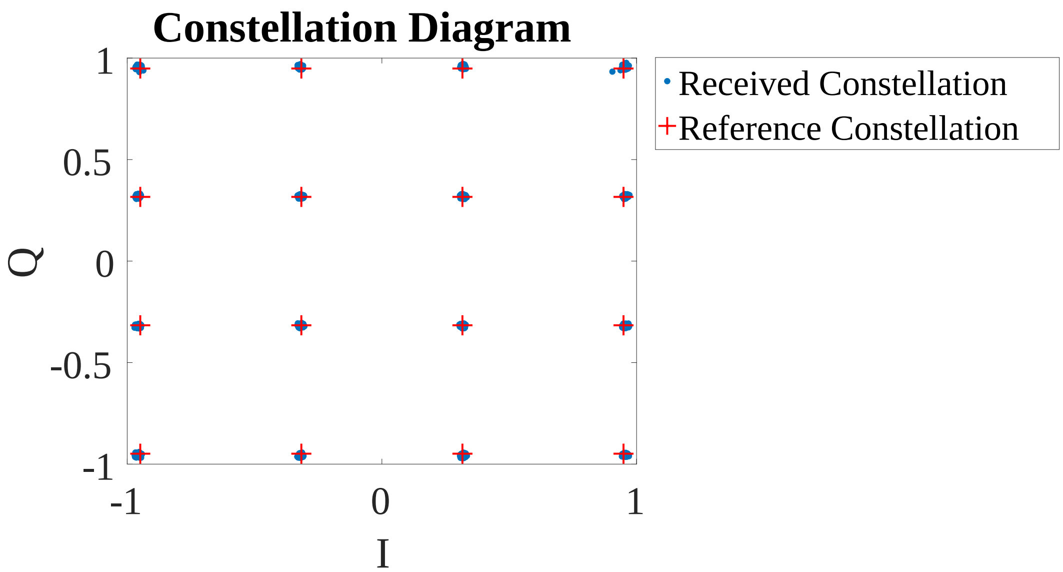

Figure 4.7: Single-carrier constellation diagram of the 16-QAM signal with 2500 symbols, 10 samples per symbol, a roll-off $\beta = 0.2$, and a span of 10. The signal is predistorted using the GMP DPD model and subsequently amplified using the SSPA model.

Compared to the uncompensated SSPA case, the constellation points become significantly more concentrated around the ideal symbol locations after DPD compensation. The GMP-based predistorter successfully compensates for both the nonlinear amplitude distortion and the memory effects introduced by the amplifier.

The overall constellation quality is therefore substantially improved. The remaining distortion is much lower than in the uncompensated case, showing that the GMP DPD model effectively captures the dominant characteristics of the amplifier.

A summary of the baseline performance of the GMP DPD model for the SSPA case is presented in Tab. 4.5.

Table 4.5: Baseline performance metrics of the GMP DPD model cascaded with the SSPA model.

Modulation	Lower ACLR (dB)	Upper ACLR (dB)	NMSE (dB)	$\mathrm{EVM}_{\mathrm{RMS}}$ (%)
QPSK	-38.27	-37.98	-40.66	0.76
16-QAM	-37.35	-36.51	-42.94	0.78
DFT-s-OFDM	-25.06	-26.08	-27.17	0.93
CP-OFDM	-26.01	-25.44	-28.45	0.79

The results in Tab. 4.5 demonstrate that the GMP-based DPD model significantly improves the communication performance for all evaluated waveforms. The ACLR values improve substantially compared to the uncompensated SSPA case, indicating that the spectral regrowth caused by the amplifier memory effects is effectively reduced.

The EVM values are also considerably reduced for all waveforms. Although the OFDM-based signals still exhibit slightly higher EVM values than the single-carrier 16-QAM signal, the overall improvement remains significant. This suggests that the GMP DPD model successfully compensates for the dominant nonlinear memory effects present in the SSPA model.

The NMSE values further confirm the effectiveness of the DPD model. Although the SSPA case does not achieve the same NMSE performance as the memoryless TWTA case, the overall signal quality is still greatly improved compared to the uncompensated amplifier. This indicates that the GMP DPD model is capable of linearizing relatively complex amplifier behavior with a manageable number of parameters.

4.1.3.3 Baseline Performance Summary

The results demonstrate that both the TWTA and SSPA models introduce significant nonlinear distortion into the communication signals. However, the distortion characteristics differ considerably between the two amplifier types. The memoryless TWTA model introduces severe static AM/AM and AM/PM distortion, resulting in a strongly distorted signal. However, since the model does not include memory effects, its behavior is comparatively easier to compensate using a memoryless predistorter.

The SSPA model, on the other hand, introduces both nonlinear distortion and memory effects. This results in a more complex and waveform-dependent distortion behavior, as observed from the constellation diagrams and the performance metrics. Although the SSPA distortion is in some cases less severe in terms of ACLR and NMSE, the presence of memory effects makes the linearization problem more challenging.

The OFDM-based waveforms experience the largest degradation across most of the evaluated performance metrics. This behavior is closely related to their higher PAPR. Since the input signals are scaled such that the maximum signal power corresponds to the maximum input power of the PA model, waveforms with higher PAPR operate at a lower average input power. In addition, their large envelope variations make them more sensitive to nonlinear compression and memory effects.

The lower average operating power associated with high-PAPR signals also has practical implications. For a given peak power limitation, these signals transmit less average power, which can reduce the achievable communication range in free-space propagation. Furthermore, operating the amplifier with a larger power back-off generally reduces power efficiency. This illustrates the trade-off between waveform characteristics, amplifier efficiency, and linearity.

Finally, the DPD results show that both amplifier models can be effectively linearized when an appropriate predistorter structure is used. The memoryless polynomial DPD provides strong compensation for the TWTA model, while the GMP-based DPD is able to compensate for the more complex memory-dependent behavior of the SSPA model. In both cases, DPD significantly improves ACLR, NMSE, and EVM, restoring the link performance close to the ideal reference case.

4.2 Complexity Reduction Study

In this section, the relationship between DPD model complexity and linearization performance is investigated. The objective is to determine the minimum model complexity required to achieve acceptable linearization performance for the evaluated waveforms and amplifier models.

First, the memoryless polynomial DPD model is evaluated with different maximum polynomial orders when compensating for the memoryless TWTA model. Thereafter, the GMP-based DPD model is analyzed when compensating for the full GMP SSPA model. For the SSPA case, the effects of polynomial order, memory depth, and lagging/leading cross terms are investigated.

4.2.1 TWTA

The normalized mean square error (NMSE) obtained when varying the maximum polynomial order of the memoryless polynomial DPD model is shown in Fig. 4.8.

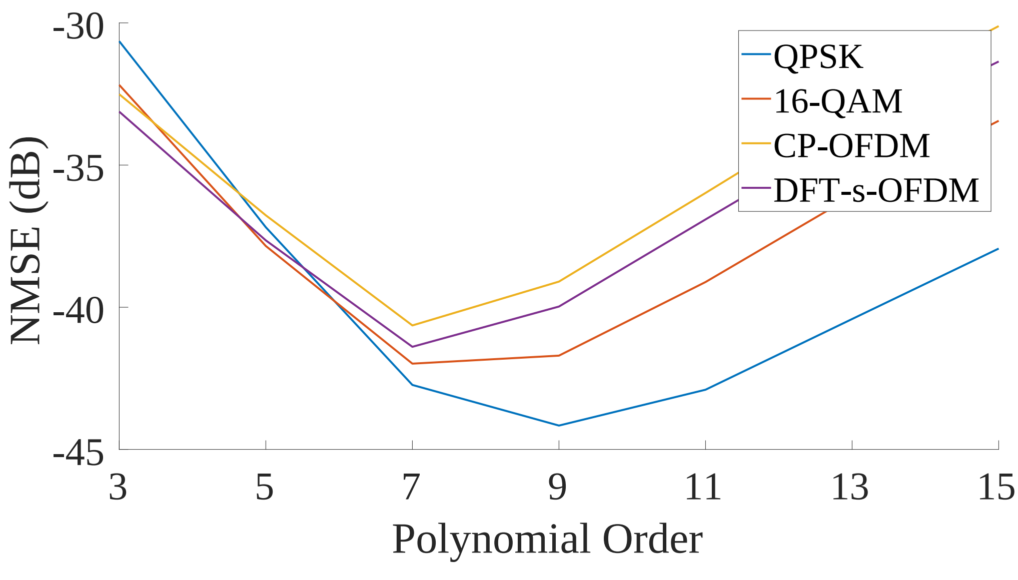

Figure 4.8: NMSE of the TWTA model cascaded with the polynomial DPD model using different maximum polynomial orders up to order 15.

As shown in Fig. 4.8, increasing the maximum polynomial order initially results in a clear improvement in NMSE for all evaluated waveforms. The most significant improvement is obtained when increasing the maximum polynomial order from 3 to 7. This indicates that the dominant nonlinear behavior of the TWTA model cannot be fully compensated by the lowest-order polynomial terms alone, and that higher-order nonlinear terms are required to accurately approximate the inverse amplifier characteristics.

For polynomial orders above 7, the NMSE improvement becomes marginal or, for several of the evaluated waveforms, begins to degrade. According to the acceptable linearization criterion defined in Section 1.2, this indicates that the performance plateau has been reached at approximately seventh order. Additional polynomial terms therefore increase the number of model coefficients without providing a corresponding improvement in linearization performance. Since the TWTA model is memoryless and has a relatively smooth AM/AM and AM/PM response, excessively high polynomial orders are not required and may instead lead to overfitting of the training data.

The ACLR obtained for varying polynomial orders is presented in Fig. 4.9.

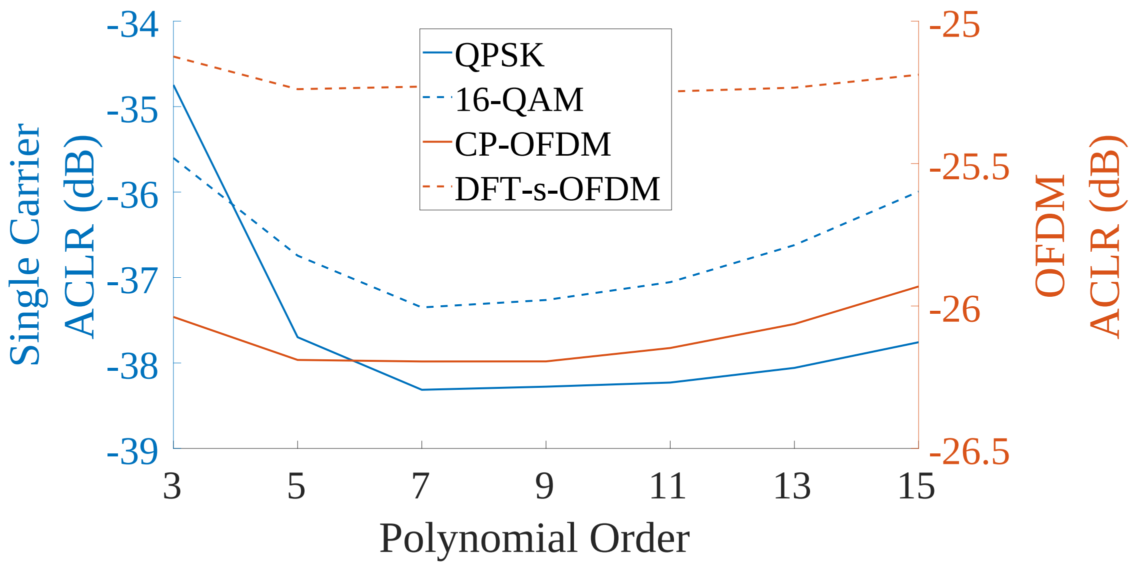

Figure 4.9: Lower ACLR of the TWTA model cascaded with the polynomial DPD model using different maximum polynomial orders. The x-axis corresponds to the maximum polynomial order used, the left y-axis corresponds to the ACLR performance of the QPSK and 16-QAM signals in dB, and the right y-axis corresponds to the ACLR performance of the CP-OFDM and DFT-s-OFDM waveforms in dB.

The ACLR behavior shown in Fig. 4.9 differs somewhat from the NMSE trend. For the OFDM-based waveforms, the ACLR remains relatively unchanged across the tested polynomial orders. This suggests that the ACLR performance for these waveforms is not primarily limited by the memoryless nonlinear distortion of the

TWTA model, but also by the inherent spectral characteristics of the OFDM signals and the selected waveform processing.

In contrast, the single-carrier waveforms show a clearer dependence on polynomial order. Increasing the maximum polynomial order improves the ACLR performance up to approximately order 7, after which the additional gains are small. For higher polynomial orders, no consistent improvement is observed, and in some cases the ACLR slightly degrades. This supports the conclusion drawn from the NMSE results: a seventh-order memoryless polynomial DPD model is sufficient to compensate the dominant TWTA nonlinearities, while higher orders do not provide meaningful additional benefit.

The EVM obtained for varying polynomial orders is shown in Fig. 4.10.

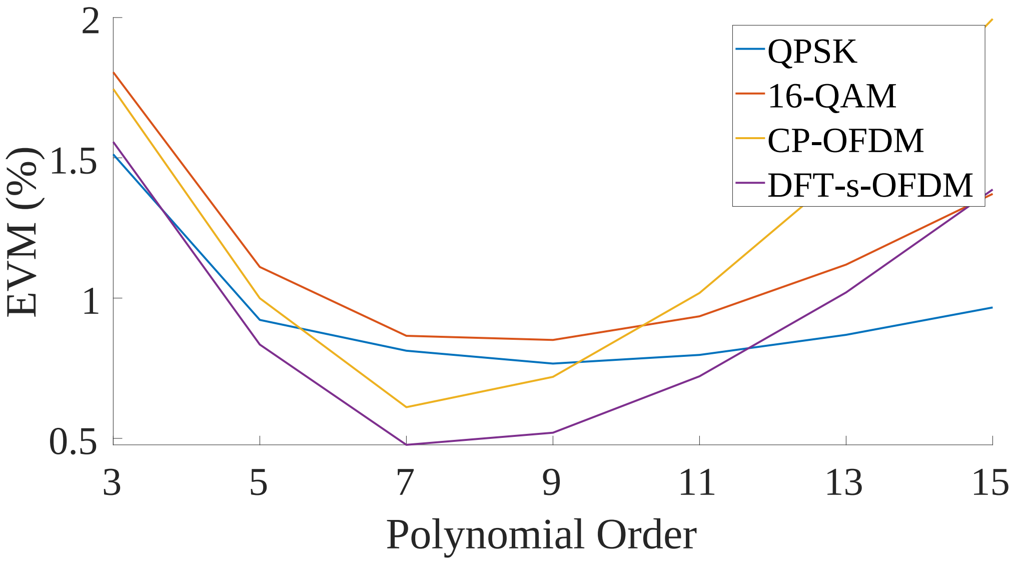

Figure 4.10: $\mathrm{EVM}_{\mathrm{RMS}}$ of the TWTA model cascaded with the polynomial DPD model using different maximum polynomial orders.

As shown in Fig. 4.10, the EVM results follow the same general trend as the NMSE results. Increasing the polynomial order substantially improves the modulation quality up to approximately order 7. Beyond this point, the EVM even deteriorates for the tested waveforms, particularly for the OFDM signals.

Overall, the TWTA complexity sweep shows that a seventh-order static polynomial DPD model is required to satisfy the defined acceptable linearization requirements across all evaluated waveforms. Lower-order models do not consistently reach the performance plateau in NMSE, ACLR, and EVM, while polynomial orders above 7 provide only marginal or ill-conditioned results. Therefore, a maximum polynomial order of 7 is selected as the minimum-complexity TWTA DPD configuration that satisfies all linearization requirements considered in this thesis.

4.2.2 SSPA

This section evaluates the complexity-performance trade-off of the GMP-based DPD model when compensating for the memory-dependent SSPA model. The effects of polynomial order, memory depth, and lagging/leading cross terms are investigated for the different waveform types.

4.2.2.1 ACLR Performance

The ACLR performance of the GMP-DPD model remains largely unchanged across the tested parameter configurations, indicating that increased model complexity yields only marginal improvements in spectral regrowth suppression. As shown in Appendix A, the difference in ACLR between the simplest configuration, a memoryless third-order model, and the most complex evaluated configuration is small for all waveforms. The maximum observed difference is approximately 2 dB.

These results suggest that the additional GMP parameters provide limited ACLR benefit under the considered operating conditions. In the present setup, spectral regrowth therefore appears to be dominated mainly by the lower-order static nonlinearities, meaning that a simple third-order static polynomial model is sufficient to suppress most of the adjacent-channel leakage.

4.2.2.2 NMSE Performance

The NMSE performance of the GMP-DPD model for the different waveform types is presented in this section.

The NMSE performance for the QPSK signal is shown in Fig. 4.11.

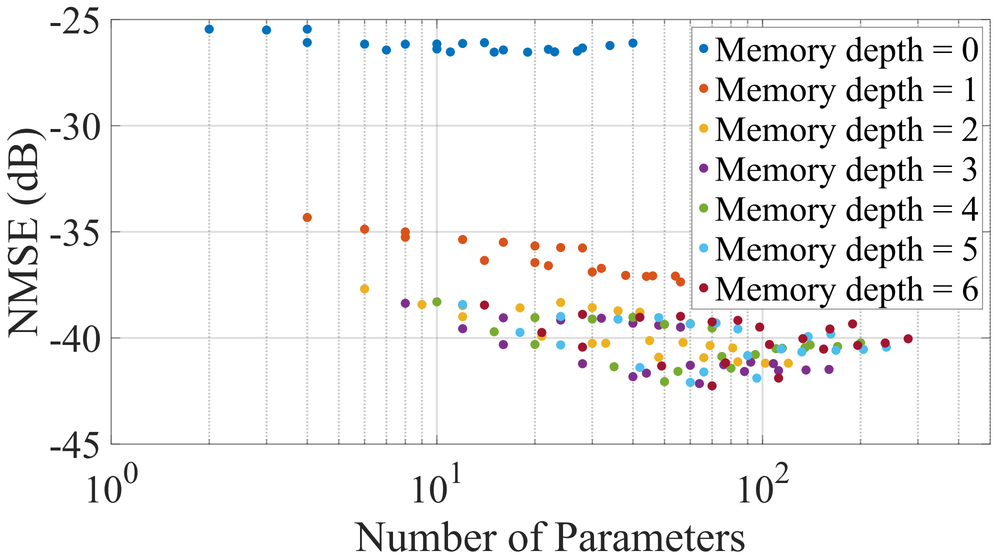

Figure 4.11: QPSK NMSE versus GMP DPD model complexity.

Fig. 4.11 shows a significant improvement in NMSE performance when moving from low-complexity models to models with increased memory depth. The most important parameter for reducing the NMSE is the memory depth. A clear improvement is observed when increasing the memory depth from $M = 0$ to $M = 2$, whereas further increases provide diminishing returns.

The figure also shows that the polynomial order and the lagging/leading cross terms have a smaller impact on the overall NMSE performance compared to the memory depth. However, the best performance is still achieved when higher-order polynomial terms and cross terms are included, indicating that these parameters provide additional refinement once the dominant memory effects have been captured.

The overall NMSE behavior for the 16-QAM signal is similar to that of the QPSK signal, as shown in Fig. 4.12.

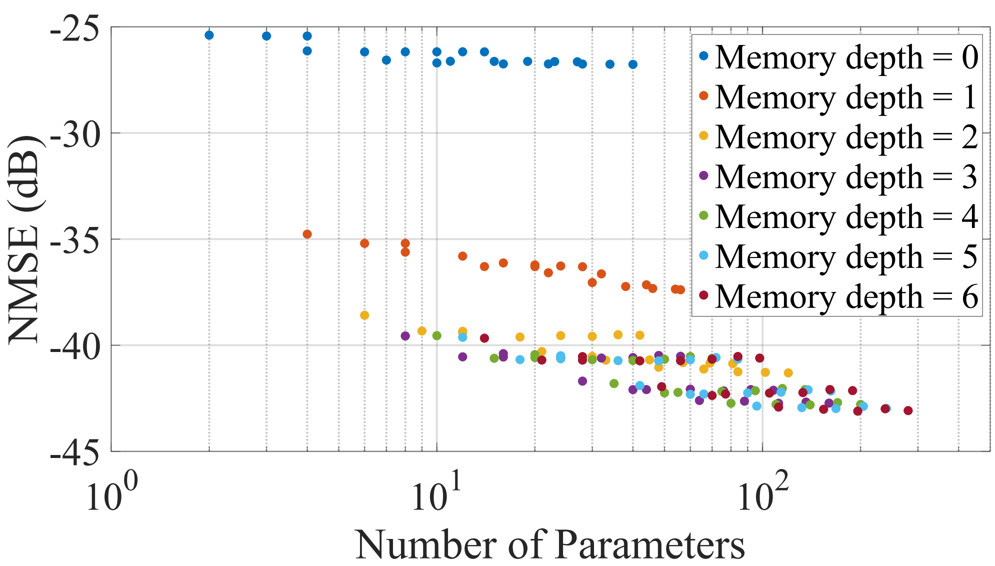

Figure 4.12: 16-QAM NMSE versus GMP DPD model complexity.

Fig. 4.12 shows that memory depth is again the dominant parameter affecting NMSE performance. Increasing the memory depth results in the largest improvement, while increasing the polynomial order and including lagging/leading cross terms provide smaller additional gains. This confirms that the dominant impairment introduced by the SSPA model is memory-dependent and must therefore be compensated using a DPD model with sufficient memory.

Compared to the single-carrier signals, the parameter sweeps for the OFDM-based waveforms exhibit a less distinct optimum. This behavior is illustrated in Fig. 4.13 and Fig. 4.14.

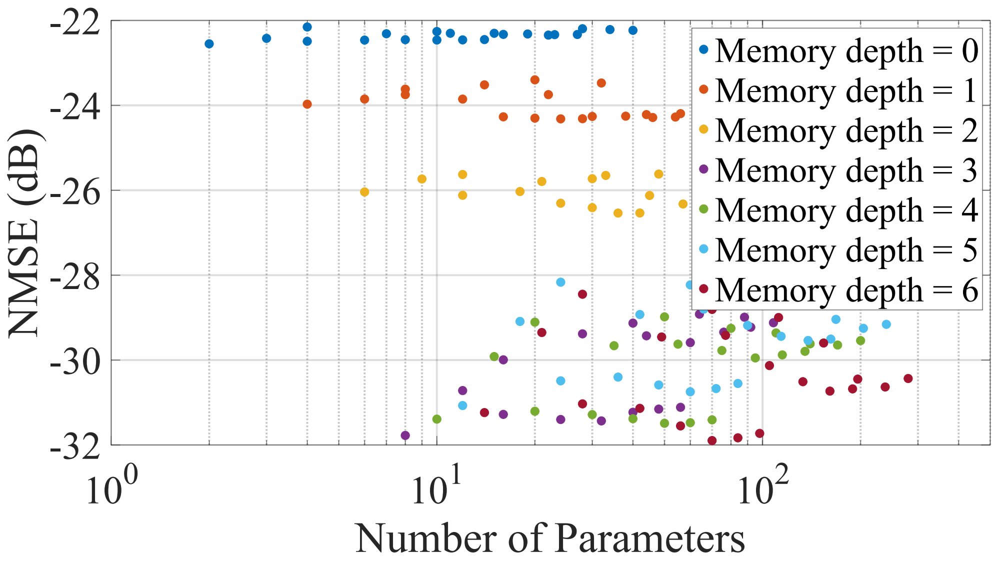

Figure 4.13: CP-OFDM NMSE versus GMP DPD model complexity.

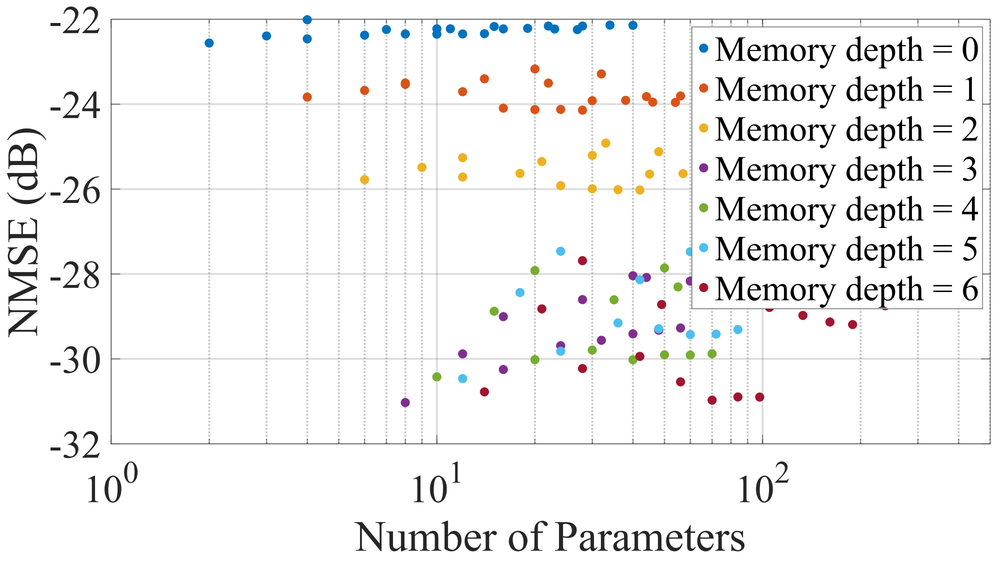

Figure 4.14: DFT-s-OFDM NMSE versus GMP DPD model complexity.

For both OFDM-based waveforms, the NMSE performance is primarily influenced by the memory depth of the GMP-DPD model. Increasing the memory depth improves the NMSE up to $M = 3$, indicating that memory effects are important for accurately compensating the PA distortion. However, further increasing the memory depth does not provide additional improvement. Instead, the NMSE starts to degrade, which may indicate overfitting.

Overall, the results show that memory depth is essential for improving the NMSE performance of the GMP-DPD model, but only up to a certain point. For the considered OFDM-based signals, a memory depth of approximately three appears to provide the best trade-off between model complexity and NMSE performance.

4.2.2.3 EVM Performance

The EVM performance of the GMP-DPD model for the different waveform types is presented in this section. First, the EVM performance for the single-carrier signals is shown in Fig. 4.15 and Fig. 4.16.

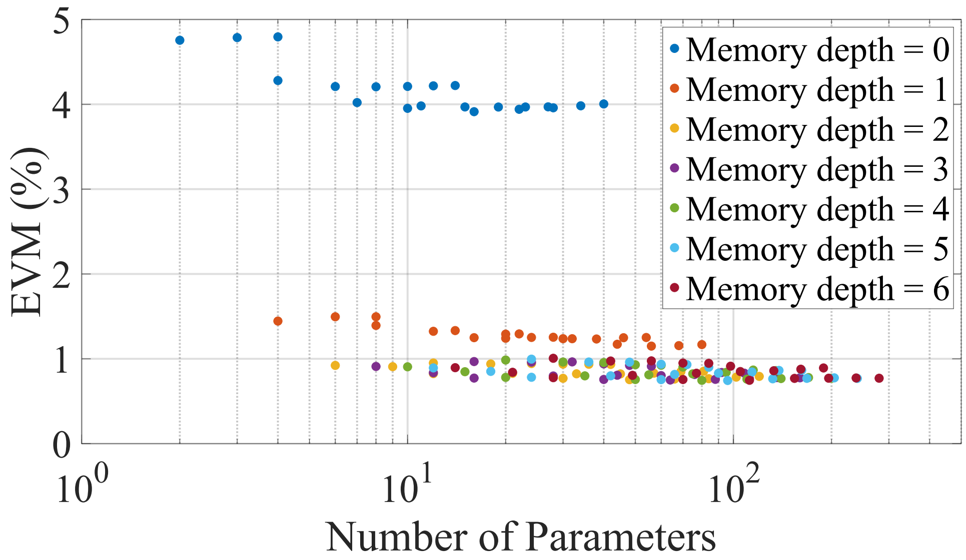

Figure 4.15: QPSK $\mathrm{EVM}_{\mathrm{RMS}}$ versus GMP DPD model complexity.

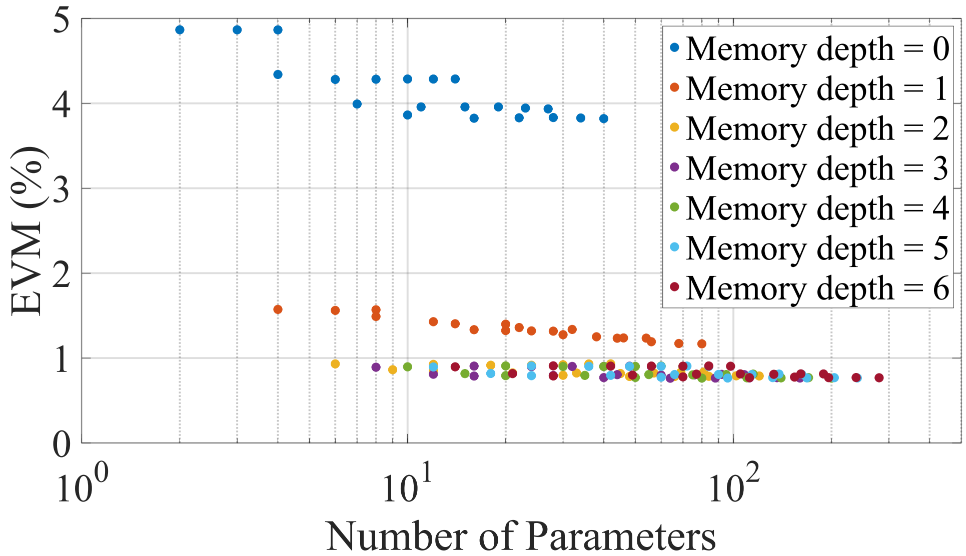

Figure 4.16: 16-QAM $\mathrm{EVM}_{\mathrm{RMS}}$ versus GMP DPD model complexity.

Fig. 4.15 and Fig. 4.16 show trends similar to those observed for the NMSE performance of the single-carrier signals. The memory depth is again the most important parameter, with the largest improvement obtained when increasing the memory depth up to $M = 2$. Beyond this point, no significant additional improvement is observed.

This indicates that a moderate memory depth is sufficient to capture the dominant memory effects affecting the constellation quality of the single-carrier signals. Higher polynomial orders and cross terms provide some additional improvement, but their impact is smaller than that of the memory depth.

Finally, the EVM results for the OFDM-based waveforms are shown in Fig. 4.17 and Fig. 4.18.

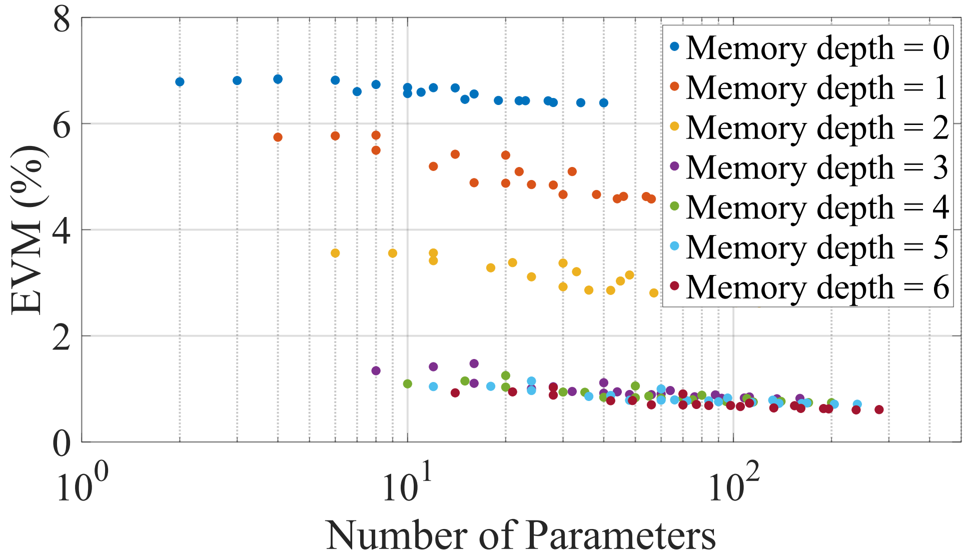

Figure 4.17: CP-OFDM EVM_{RMS} versus GMP DPD model complexity.

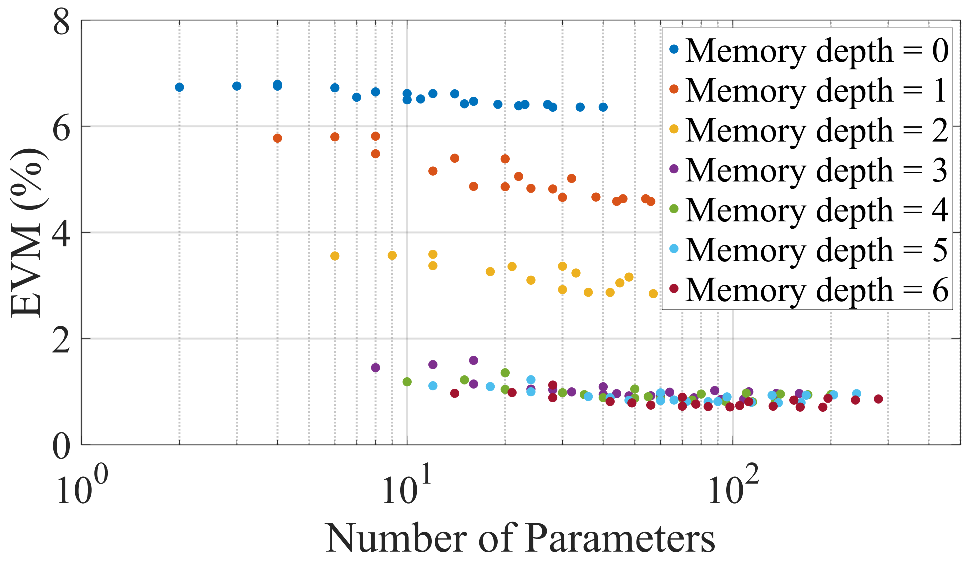

Figure 4.18: DFT-s-OFDM $\mathrm{EVM}_{\mathrm{RMS}}$ versus GMP DPD model complexity.

Both the CP-OFDM signal shown in Fig. 4.17 and the DFT-s-OFDM signal shown in Fig. 4.18 exhibit a strong dependence on memory depth. A major improvement is observed when increasing the memory depth up to approximately $M = 3$, with some additional improvement observed up to $M = 6$.

This suggests that, for OFDM-based waveforms, the DPD model may require a larger memory depth than the GMP PA model itself in order to achieve the best linearization performance. This can be explained by the larger envelope variations and higher PAPR of the OFDM signals, which make them more sensitive to memory-dependent nonlinear distortion.

Fig. 4.17 and Fig. 4.18 also show that higher polynomial orders and lagging/leading cross terms contribute to the EVM performance, although their impact is smaller than that of the memory depth. Thus, while these additional terms can improve the final performance, the memory depth remains the primary factor determining the effectiveness of this GMP-DPD model.

4.2.2.4 SSPA Complexity Trade-off Summary

To summarize the SSPA complexity reduction study, memory depth is the most important parameter for the considered GMP-based PA model. Increasing the memory depth provides the largest improvements in both NMSE and EVM, especially for the EVM of the OFDM-based waveforms. In some cases, using a DPD memory depth larger than that of the GMP PA model provides additional performance gains, indicating that the inverse model may require a more extensive memory representation than the amplifier model.

Although memory depth is the dominant parameter, additional improvements are obtained by increasing the polynomial order and including lagging/leading cross terms. These parameters are particularly useful for refining the compensation once the main memory effects have been captured. However, their contribution is generally smaller than that of the memory depth.

The ACLR results show only limited sensitivity to the tested complexity configurations, with less than 2 dB difference between the simplest and most complex models. This indicates that, for the evaluated conditions, increasing the GMP-DPD complexity mainly improves in-band signal quality, as reflected by NMSE and EVM, rather than adjacent-channel leakage.

Overall, the results show that the required DPD complexity depends on both the amplifier model and the waveform type. For the memoryless TWTA model, a seventh-order memoryless polynomial DPD is required to satisfy the acceptable linearization requirements across all evaluated waveforms. Lower polynomial orders do not consistently reach the performance plateau, while higher orders provide only marginal or inconsistent results due to overfitting.

For the memory-dependent SSPA model, the results show that memory depth is the dominant complexity parameter. Increasing the memory depth provides the most important improvement in linearization performance, particularly for the OFDM-based waveforms where in-band distortion is more pronounced. In contrast, increasing the maximum polynomial order beyond third order and adding lagging or leading cross terms provides only limited additional benefit relative to the increase in model complexity.

Based on the acceptable linearization criterion used in this thesis, the minimum-complexity SSPA DPD configuration is therefore selected as a memory polynomial model with a memory depth of $M = 3$, a maximum polynomial order of $K = 3$, and no lagging or leading cross terms. Since only odd polynomial orders are included, this corresponds to the linear and third-order terms. With four memory taps, ($m=0,1,2,3$), the resulting model contains ($2 \times 4 = 8$) coefficients. This configuration satisfies the acceptable linearity constraints according to the defined performance-plateau criterion, although higher memory depths can provide additional waveform-specific EVM improvements for the OFDM-based signals. Consequently, the complexity reduction study indicates that, for the considered SSPA case, model reduction should prioritize retaining sufficient memory depth, while higher polynomial orders and cross terms should only be included if additional waveform-specific performance margins are required.

4.3 Noise Robustness Analysis

In this section, the robustness of the DPD models against additive noise is evaluated. Two noise scenarios are considered. In the first scenario, noise is added to the input signal between predistortion and amplification. This represents degradation of the transmitted baseband signal itself.

In the second scenario, noise is added to the PA output used during DPD training. This represents measurement noise in the feedback path. The objective is to investigate whether the trained DPD models remain effective when either the operating signal or the training data is corrupted by noise.

4.3.1 Input noise

The EVM results for the TWTA case with input noise are shown in Fig. 4.19. As expected, the EVM increases as the input SNR is reduced. This degradation is observed for all waveform types, since the input noise is passed through both the DPD model and the amplifier. At high SNR levels, the EVM approaches the corresponding baseline DPD performance, indicating that the residual error is mainly dominated by remaining nonlinear distortion and receiver imperfections. As the SNR decreases, the additive noise becomes the dominant impairment and the performance of all signals gradually deteriorates.

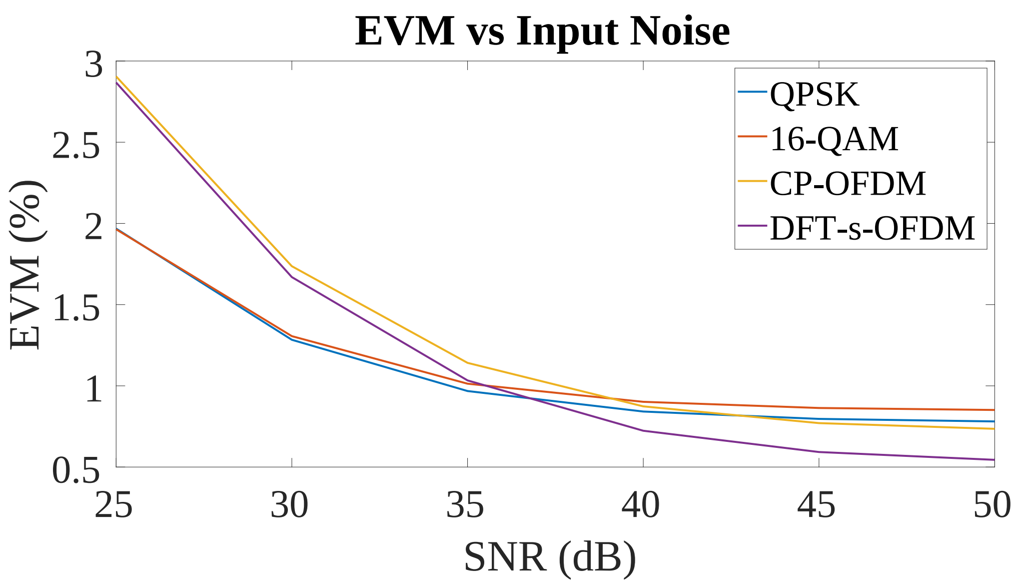

Figure 4.19: EVM_{RMS} of the TWTA for the different signals when input noise is applied.

The single-carrier waveforms remain relatively robust over a wider SNR range, whereas the OFDM-based waveforms generally exhibit stronger sensitivity to input noise. This is consistent with their higher PAPR and increased sensitivity to amplitude and phase perturbations. Nevertheless, the DPD model does not become unstable when input noise is introduced. Instead, the observed degradation is primarily caused by the additive noise itself.

For the SSPA case, shown in Fig. 4.20, a similar trend can be observed. The EVM increases with decreasing input SNR for all evaluated signals. Compared to the TWTA case, the SSPA results show slightly higher sensitivity due to the presence of memory effects in the amplifier model. These memory effects cause the input noise to influence not only the instantaneous sample, but also the effective nonlinear response over several samples. Consequently, the OFDM-based waveforms show a more noticeable degradation.

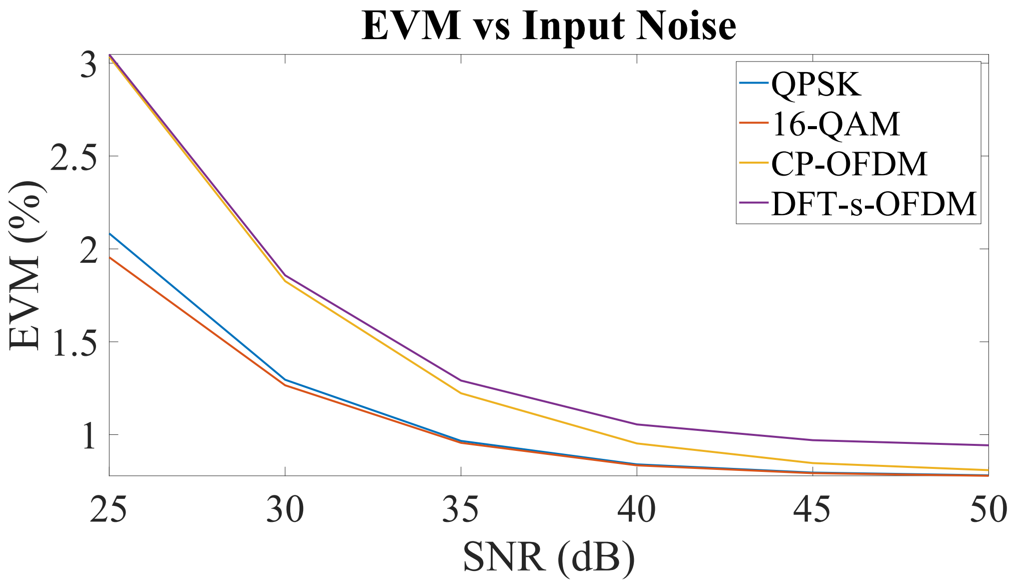

Figure 4.20: EVM_{RMS} of the SSPA for the different signals when input noise is applied.

Overall, the input-noise results show that the DPD models remain effective as long as the input SNR is sufficiently high. At lower SNR values, the communication performance becomes increasingly noise-limited, meaning that further improvements in nonlinear compensation cannot significantly reduce the EVM.

4.3.2 Output training noise

The EVM results for the TWTA model when the DPD is trained using noisy output data are presented in Fig. 4.21. In this case, the noise affects the coefficient estimation rather than the transmitted signal directly. At high training SNR values, the DPD model achieves performance close to the noiseless training baseline. This indicates that the polynomial DPD model can accurately identify the inverse TWTA characteristics when the feedback signal is only weakly corrupted by noise.

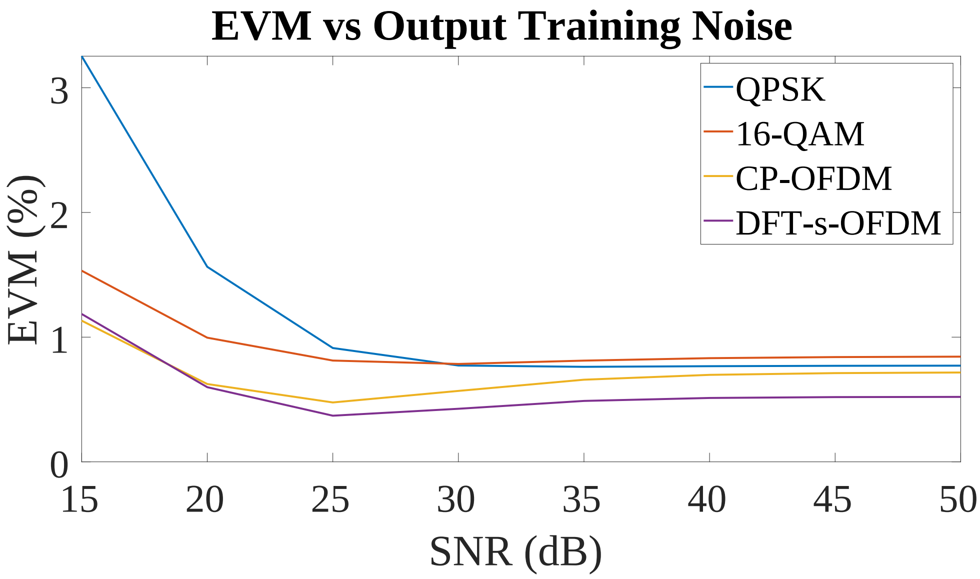

Figure 4.21: EVM_{RMS} of the TWTA for the different signals when the DPD is trained using noisy output data.

As the training SNR is reduced, the EVM increases slightly. This degradation occurs because the least-squares coefficient estimation begins to fit both the amplifier distortion and the noise component present in the measured output signal. As a result, the extracted predistorter coefficients become less accurate. However, the TWTA case remains relatively robust, since the amplifier is memoryless and the polynomial DPD model contains a limited number of coefficients. The reduced model complexity makes the coefficient estimation less sensitive to noisy training data.

The only exception is the QPSK signal below an SNR of 20 dB, where a significant performance degradation is observed. At an SNR of 15 dB, the QPSK signal reaches an EVM above 3%. This may be explained by its lower PAPR, which results in a larger portion of the signal operating closer to the amplifier compression region. Consequently, the signal becomes more sensitive to noise at lower SNR levels.

Finally, the slight decrease in EVM between 20 and 30 dB training SNR for the 16-QAM, DFT-s-OFDM, and CP-OFDM signals may be attributed to the interaction between measurement noise and the least-squares coefficient estimation used during DPD training. At moderate noise levels, the added output noise can slightly regularize the coefficient extraction by reducing the tendency of the model to fit small signal-specific variations or numerical imperfections in the training data. As a result, the estimated predistorter coefficients may generalize slightly better to the evaluated signal, producing a small improvement in EVM. However, this effect is not expected to be systematic and should be interpreted as a minor variation rather than a fundamental performance gain.

The corresponding SSPA results are shown in Fig. 4.22. In this case, the impact of output training noise is more pronounced. The GMP-DPD model contains memory terms and lagging/leading cross terms, resulting in a larger number of coefficients that must be estimated from the measured data. When the training data is noisy, the coefficient estimation therefore becomes more sensitive to measurement errors.

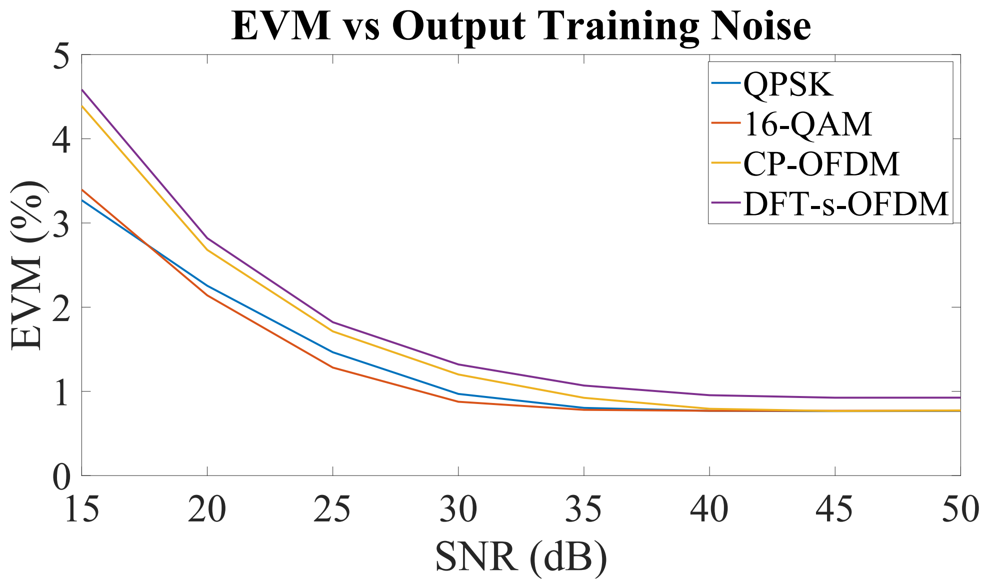

Figure 4.22: $\mathrm{EVM}_{\mathrm{RMS}}$ of the SSPA for the different signals when the DPD is trained using noisy output data.

The OFDM-based waveforms are again among the most sensitive cases. Their wider amplitude distribution and higher PAPR require accurate modeling of both nonlinear and memory-dependent behavior. When the feedback measurement is noisy, the extracted GMP coefficients become less accurate, leading to increased residual distortion after predistortion.

At training SNR values above approximately 30 dB, the extracted coefficients are sufficiently accurate and the performance improvement begins to saturate. This indicates that, beyond this point, further increases in feedback SNR provide diminishing returns, since the remaining EVM is mainly limited by residual model mismatch and receiver imperfections rather than by coefficient-estimation noise.

In summary, the output-training-noise results demonstrate that feedback measurement quality is important for reliable DPD identification. The memoryless TWTA predistorter remains relatively robust to noisy training data, while the GMP-based SSPA predistorter is more sensitive due to its higher model complexity and memory-dependent structure.

4.4 Model Mismatch and Generalization

This section evaluates the ability of the trained DPD models to generalize when the amplifier characteristics deviate from the model used during training. In practical systems, such deviations may occur due to temperature changes, component aging, bias variations, operating-point drift or even the usage of another power amplifier. The DPD model is therefore evaluated under several controlled mismatch scenarios for both the TWTA and SSPA amplifier models.

4.4.1 TWTA

The EVM results for the mismatched TWTA cases are presented in Tab. 4.6, while the corresponding NMSE results are shown in Tab. 4.7.

Table 4.6: EVM_{RMS} in % of the mismatched TWTA using the four evaluated signals: QPSK, 16-QAM, CP-OFDM, and DFT-s-OFDM.

Modulation	QPSK	16-QAM	CP-OFDM	DFT-s-OFDM
Baseline	0.77	0.86	0.72	0.52
+1 dB linear gain drift	0.77	0.86	0.72	0.52
-1 dB linear gain drift	0.77	0.86	0.72	0.52
+5 % P1dB drift	0.78	0.93	0.79	0.59
-5 % P1dB drift	0.78	0.89	0.78	0.58
+5 % AM/PM	0.81	0.96	0.92	0.67
-5 % AM/PM	0.78	0.84	0.63	0.48
Random 2 % impairment	0.78	0.88	0.75	0.55
Random 5 % impairment	0.83	0.97	0.88	0.63

Table 4.7: Normalized Mean Square Error in dB of the mismatched TWTA using the four evaluated signals: QPSK, 16-QAM, CP-OFDM, and DFT-s-OFDM.

Modulation	QPSK	16-QAM	CP-OFDM	DFT-s-OFDM
Baseline	-44.16	-41.70	-39.10	-39.98
+1 dB linear gain drift	-44.16	-41.70	-39.10	-39.98
-1 dB linear gain drift	-44.16	-41.70	-39.10	-39.98
+5 % P1dB drift	-37.79	-37.70	-36.96	-37.43
-5 % P1dB drift	-37.83	-37.68	-36.96	-37.45
+5 % AM/PM	-42.39	-39.99	-37.57	-38.54
-5 % AM/PM	-43.48	-42.27	-39.88	-40.73
Random 2 % impairment	-42.09	-40.57	-38.53	-39.29
Random 5 % impairment	-38.53	-38.10	-36.63	-37.84

For the TWTA model, the DPD performance remains highly robust under the evaluated mismatch conditions. A ± 1 dB linear gain drift has no visible impact on either EVM or NMSE. This is expected since the receiver normalization compensates for most of the linear amplitude scaling, and the nonlinear shape of the amplifier characteristic remains unchanged.

The P1dB drift has a more visible impact on the NMSE, reducing the linearization accuracy compared to the nominal case. However, the EVM degradation remains small for all waveforms. This indicates that the predistorter still compensates the dominant nonlinear behavior sufficiently well, even when the compression point of the amplifier is shifted.

The AM/PM mismatch mainly affects the phase response of the amplifier. The results show that a positive AM/PM drift causes a slightly larger degradation than a negative drift, particularly for the OFDM-based waveforms. This suggests that the trained DPD model is more sensitive to an increase in nonlinear phase rotation than to a corresponding reduction. Nevertheless, the overall EVM remains low, demonstrating that the polynomial DPD model generalizes well to moderate AM/PM variations.

The random impairment cases further confirm the robustness of the TWTA DPD model. A 2% random impairment produces only a minor degradation, while the 5% impairment results in a clearer NMSE penalty. Even in this case, the EVM values remain close to the baseline DPD results. Overall, the TWTA mismatch study shows that the memoryless polynomial DPD model is robust to moderate parameter variations and maintains good linearization performance across all evaluated waveforms.

4.4.2 SSPA

The EVM and NMSE results for the mismatched SSPA cases are presented in Tab. 4.8 and Tab. 4.9, respectively.

Table 4.8: $\mathrm{EVM}_{\mathrm{RMS}}$ in % of the mismatched SSPA using the four evaluated signals: QPSK, 16-QAM, CP-OFDM, and DFT-s-OFDM.

Modulation	QPSK	16-QAM	CP-OFDM	DFT-s-OFDM
Baseline	0.78	0.76	0.79	0.93
+1 dB linear gain drift	0.94	0.95	1.04	1.10
-1 dB linear gain drift	0.95	1.07	1.29	1.34
+1 dB linear memory drift	0.93	1.02	1.06	1.16
-1 dB linear memory drift	0.91	0.86	1.11	1.22
+5 % static nonlinear drift	0.90	1.02	1.14	1.12
-5 % static nonlinear drift	0.90	0.88	1.00	1.10
+5 % nonlinear memory drift	1.99	2.18	3.76	3.71
-5 % nonlinear memory drift	2.20	2.48	3.64	3.49
+5 % lagging/leading drift	1.97	2.10	3.31	3.23
-5 % lagging/leading drift	1.83	1.91	3.53	3.53
+3 deg nonlinear phase shift	0.80	0.80	0.85	0.99
-3 deg nonlinear phase shift	0.80	0.85	0.87	0.96
Random 2 % impairment	1.73	1.98	3.06	2.91
Random 5 % impairment	3.93	3.88	7.58	7.50

Table 4.9: Normalized Mean Square Error in dB of the mismatched SSPA using the four evaluated signals: QPSK, 16-QAM, CP-OFDM, and DFT-s-OFDM.

Modulation	QPSK	16-QAM	CP-OFDM	DFT-s-OFDM
Baseline	-40.66	-42.94	-28.45	-27.17
+1 dB linear gain drift	-35.77	-35.21	-28.44	-27.41
-1 dB linear gain drift	-35.04	-34.67	-26.99	-25.90
+1 dB linear memory drift	-28.89	-29.30	-26.07	-25.22
-1 dB linear memory drift	-29.78	-29.93	-26.92	-26.05
+5 % static nonlinear drift	-37.98	-38.68	-27.85	-26.73
-5 % static nonlinear drift	-39.21	-41.16	-28.58	-27.33
+5 % nonlinear memory drift	-27.26	-27.96	-24.32	-23.82
-5 % nonlinear memory drift	-26.05	-27.05	-24.58	-24.30
+5 % lagging/leading drift	-28.14	-29.24	-25.39	-24.96
-5 % lagging/leading drift	-29.12	-29.80	-24.69	-24.11
+3 deg nonlinear phase shift	-40.42	-42.66	-28.46	-27.19
-3 deg nonlinear phase shift	-39.94	-41.45	-28.34	-27.09
Random 2 % impairment	-30.46	-29.83	-25.13	-24.72
Random 5 % impairment	-21.82	-22.91	-19.75	-19.81

Compared to the TWTA case, the SSPA model exhibits a stronger sensitivity to parameter mismatch. This is expected since the GMP-based SSPA includes both nonlinear and memory-dependent behavior. A mismatch in the memory terms affects not only the instantaneous amplifier response but also the relationship between neighboring samples, making the predistortion problem more difficult.

The linear gain drift cases produce moderate degradation, especially for the OFDM-based waveforms. The negative gain drift results in slightly higher EVM than the positive drift, indicating that the trained predistorter is somewhat more sensitive when the amplifier gain is reduced. The linear memory drift also affects the OFDM-based signals more strongly than the single-carrier signals, which is consistent with their higher sensitivity to memory-dependent distortion.

The static nonlinear drift has only a limited impact on performance. Both EVM and NMSE remain close to the nominal DPD case, especially for the single-carrier waveforms. This suggests that the GMP DPD model can tolerate moderate changes in the static nonlinear coefficients.

In contrast, the nonlinear memory drift and lagging/leading drift cases cause a much larger degradation. These impairments directly affect the dynamic nonlinear behavior that the GMP DPD model is designed to compensate. Since the predistorter was trained for the nominal memory structure, changes in these terms lead to residual distortion that cannot be fully corrected. This effect is especially visible for CP-OFDM and DFT-s-OFDM, where the EVM increases substantially compared to the nominal DPD baseline.

The nonlinear phase-shift cases have a relatively small effect compared to the nonlinear memory mismatch. This indicates that the evaluated phase perturbation is less critical than errors in the dynamic nonlinear coefficients. However, some degradation is still observed, particularly for the OFDM-based signals.

The random impairment cases summarize the overall sensitivity of the SSPA DPD model to combined parameter variations. A 2% random impairment already produces noticeable degradation, while the 5% random impairment results in severe performance loss, even making the frame synchronization of the QPSK unreliable. This confirms that the GMP-based DPD model is significantly more sensitive to model mismatch than the memoryless TWTA predistorter.

Overall, the model mismatch results show that the DPD models generalize well when the amplifier deviations are moderate. The TWTA case is highly robust due to the relatively simple memoryless amplifier behavior. The SSPA case is substantially more sensitive, particularly to nonlinear memory and lagging/leading coefficient variations.

4.5 Limitations and Future Work

The main limitations of this thesis stem from confidentiality constraints, which affected both the evaluation methodology and the choice of waveforms. Specifically, the evaluation was conducted using behavioral models rather than direct measurements from operational hardware systems. Although these models were selected to emulate realistic amplifier behavior, they cannot fully capture all practical impairments present in real RF hardware. In addition, the waveforms used in the evaluation were limited to general single-carrier and multi-carrier waveforms, rather than proprietary or application-specific signal formats.

Due to these limitations, several possible extensions of this work can be identified. An important next step would be to validate the proposed DPD models using the actual communication waveforms used at Saab, together with the intended radar functionality. This would make it possible to evaluate the DPD performance under realistic joint radar-communication operation and verify that the combined use of the waveforms does not degrade the linearization performance.

A second step would be to characterize and validate the specific TWTA and SSPA used at Saab. This should include verifying that the amplifiers are sufficiently invertible within their intended operating regions, since DPD relies on the possibility of approximating the inverse behavior of the PA. During this characterization, measured PA input-output data should also be collected and stored. Such a database would simplify future testing, benchmarking, and validation of different DPD models without requiring repeated hardware measurements.

The amplifier characterization should also be used to investigate the presence of memory effects for the relevant waveforms and operating conditions. This is particularly important for the TWTA, where it should be verified whether the memoryless assumption used in this work remains valid for the actual Saab use case. If the TWTA does not exhibit significant memory effects, then a relatively simple DPD structure may be sufficient. For the SSPA, however, the results in Section 4.4.2 indicate that memory effects and random impairments can have a stronger influence, which should be considered in future implementations.

Once both the software and hardware validation have been completed, a more advanced DPD implementation could be developed. Two suitable alternatives are a look-up-table (LUT) based DPD and an adaptive DPD implementation. The choice between these approaches should depend on the measured amplifier behavior, the required linearization performance, and the available implementation resources.

A LUT-based DPD is attractive due to its relatively low implementation complexity [7], [30]. In such an implementation, the predistortion coefficients are stored in a table and selected based on parameters such as input amplitude, operating point, temperature, or frequency [30], [31]. However, LUT-based DPDs are often implemented as memoryless models, which limits their ability to compensate for dynamic PA behavior [31]–[33]. Since memory effects are more sensitive to operating conditions and random impairments, as shown in Section 4.4.2, a LUT-based DPD is likely most suitable for the TWTA, provided that the TWTA can be shown to have negligible memory effects for the relevant waveform and operating region [3], [34].

An adaptive DPD, on the other hand, can track changes in the PA behavior over time [7], [35], [36]. This includes variations due to temperature, supply voltage, frequency, load mismatch, aging, and output power level [36], [37]. Adaptive predistortion normally requires an observation path, including feedback, demodulation, ADC conversion, and an adaptation algorithm [35], [36]. This makes the implementation significantly more complex than a fixed LUT-based DPD. However, it also provides higher robustness and can be extended to include memory effects [6], [33], [36]. For this reason, an adaptive DPD is likely the more suitable alternative for the SSPA, where memory effects and operating-condition-dependent behavior must be captured more accurately [6], [10], [11].

5
Conclusion

This thesis has investigated digital predistortion as a software-based method for mitigating power amplifier nonlinearities in communication signals transmitted through a radar-optimized shared aperture. The objective was to evaluate whether DPD can improve communication performance without modification of the RF hardware, and to determine how the complexity of the predistortion model should be selected for different amplifier characteristics and waveform types.

The study considered two amplifier models: a memoryless Saleh model representing a traveling-wave tube amplifier, and a generalized memory polynomial model representing a solid-state power amplifier with nonlinear memory effects. Four communication waveforms were evaluated: QPSK, 16-QAM, CP-OFDM, and DFT-s-OFDM. Performance was assessed using EVM, ACLR, and NMSE.

The results show that nonlinear PA operation can significantly degrade communication performance through both in-band distortion and spectral regrowth. The severity of this degradation depends on both the waveform and the amplifier model. In general, the OFDM-based waveforms were more sensitive to nonlinear distortion than the single-carrier waveforms, which is consistent with their higher PAPR. The SSPA model also produced more complex distortion than the TWTA model due to its nonlinear memory effects.

Digital predistortion was shown to substantially reduce the distortion introduced by both amplifier models. For the memoryless TWTA case, a static polynomial predistorter was sufficient to compensate for the dominant AM/AM and AM/PM distortion. Increasing the polynomial order improved performance only up to a certain point, after which further increases led to diminishing returns and ill-conditioned results. For the evaluated TWTA case, a seventh-order memoryless polynomial model provided the best overall result.

For the memory-dependent SSPA case, the results show that a memory-based polynomial DPD is required to compensate for the nonlinear dynamic behavior. Among the investigated parameters, memory depth was found to be the most important factor for improving EVM and NMSE performance, particularly for the OFDM-based waveforms. Higher polynomial order and the inclusion of lagging and leading cross terms also improved performance, but their contribution was generally smaller and showed clearer diminishing returns. This indicates that memory depth should be prioritized when selecting the complexity of the DPD model.

The primary research question concerned the minimum-complexity DPD model required to achieve acceptable linearization performance under nonlinear PA distortion and noise. The results indicate that this model should not be defined by a fixed universal parameter set. Instead, the appropriate complexity should be selected based on the point where further increases provide only marginal improvements in EVM, ACLR, and NMSE. For memoryless amplifier behavior, this point can be reached with a low-complexity memoryless polynomial model. For amplifiers with nonlinear memory effects, sufficient memory depth is the dominant requirement, while higher polynomial order and cross terms should be added only until the performance reaches a clear plateau.

The robustness and model mismatch analyses show that DPD remains effective under moderate noise levels and moderate variations in amplifier behavior. However, performance degrades as the SNR decreases or as the feedback signal used for training becomes less accurate. The TWTA predistorter was relatively robust to parameter variations, while the SSPA predistorter was more sensitive, especially to variations in the nonlinear memory coefficients and cross terms. This suggests that practical GMP-based DPD implementations require accurate amplifier characterization and may benefit from periodic retraining or adaptive coefficient updates.

Overall, the thesis demonstrates that digital predistortion is a promising approach for improving communication performance in radar-communication shared aperture systems. For amplifiers dominated by memoryless nonlinearities, a low-complexity polynomial predistorter can provide sufficient linearization. For the amplifier with nonlinear memory effects, an MP-based predistorter is needed, with memory depth being the most important complexity parameter. The results support the conclusion that software-based linearization can improve modulation quality and spectral behavior without requiring changes to the RF hardware.

Future work should proceed from realistic joint waveform validation, to hardware characterization, and finally to the implementation of DPD architectures adapted to each amplifier type. A LUT-based DPD appears promising for the TWTA if memory effects are negligible, while an adaptive DPD is likely required for the SSPA to achieve sufficient linearization under realistic operating conditions.

Bibliography

[1] P. M. Lavrador, T. R. Cunha, P. M. Cabral, and J. Pedro, "The linearity-efficiency compromise," *IEEE Microwave Magazine*, vol. 11, no. 5, pp. 44–58, 2010. DOI: 10.1109/MMM.2010.937100.

[2] S. C. Cripps, *RF Power Amplifiers for Wireless Communications*, 2nd ed. Artech House, 2006, ISBN: 9781596930186.

[3] A. Saleh, "Frequency-independent and frequency-dependent nonlinear models of twt amplifiers," *IEEE Transactions on Communications*, vol. 29, no. 11, pp. 1715–1720, 1981. DOI: 10.1109/TCOM.1981.1094911.

[4] J. P. Aikio and T. Rahkonen, "A comprehensive analysis of am–am and am–pm conversion in an ldmos rf power amplifier," *IEEE Transactions on Microwave Theory and Techniques*, vol. 57, no. 2, pp. 262–270, 2009. DOI: 10.1109/TMTT.2008.2011161.

[5] L. Ding et al., "A robust digital baseband predistorter constructed using memory polynomials," *IEEE Transactions on Communications*, vol. 52, no. 1, pp. 159–165, 2004. DOI: 10.1109/TCOMM.2003.822188.

[6] D. Morgan, Z. Ma, J. Kim, M. Zierdt, and J. Pastalan, "A generalized memory polynomial model for digital predistortion of rf power amplifiers," *IEEE Transactions on Signal Processing*, vol. 54, no. 10, pp. 3852–3860, 2006. DOI: 10.1109/TSP.2006.879264.

[7] J. K. Cavers, "Amplifier linearization using a digital predistorter with fast adaptation and low memory requirements," *IEEE Transactions on Vehicular Technology*, vol. 39, no. 4, pp. 374–382, 1990. DOI: 10.1109/25.61359.

[8] C. Eun and E. J. Powers, "A new volterra predistorter based on the indirect learning architecture," *IEEE Transactions on Signal Processing*, vol. 45, no. 1, pp. 223–227, 1997. DOI: 10.1109/78.552219.

[9] F. M. Ghannouchi, O. Hammi, and M. Helaoui, *Behavioral Modeling and Predistortion of Wideband Wireless Transmitters*. John Wiley & Sons, 2015, ISBN: 9781118406274. DOI: 10.1002/9781119004424.

[10] J. Vuolevi, T. Rahkonen, and J. Manninen, "Measurement technique for characterizing memory effects in rf power amplifiers," *IEEE Transactions on Microwave Theory and Techniques*, vol. 49, no. 8, pp. 1383–1389, 2001. DOI: 10.1109/22.939917.

[11] H. Ku, M. D. McKinley, and J. S. Kenney, "Quantifying memory effects in rf power amplifiers," *IEEE Transactions on Microwave Theory and Techniques*, vol. 50, no. 12, pp. 2843–2849, 2002. DOI: 10.1109/TMTT.2002.805196.

[12] T. Liu, S. Boumaiza, A. B. Sesay, and F. M. Ghannouchi, "Quantitative measurements of memory effects in wideband rf power amplifiers driven by modulated signals," *IEEE Microwave and Wireless Components Letters*, vol. 17, no. 1, pp. 79–81, 2007.

[13] A. Zaidi, F. Athley, J. Medbo, U. Gustavsson, G. Durisi, and X. Chen, *5G Physical Layer: Principles, Models and Technology Components*. Academic Press, 2018, ch. 4, pp. 87–118. DOI: 10.1016/C2017-0-01973-0.

[14] 3GPP, "NR; Base Station (BS) Conformance Testing; Part 1: Conducted Conformance Testing," 3rd Generation Partnership Project (3GPP), Technical Specification TS 38.141-1, 2026, Under change control; accessed 2026-06-17. [Online]. Available: https://www.3gpp.org/dynareport/38141-1.htm.

[15] J. C. Pedro and S. A. Maas, "A comparative overview of microwave and wireless power-amplifier behavioral modeling approaches," *IEEE Transactions on Microwave Theory and Techniques*, vol. 53, no. 4, pp. 1150–1163, 2005. DOI: 10.1109/TMTT.2005.845723.

[16] J. Kim and K. Konstantinou, "Digital predistortion of wideband signals based on power amplifier model with memory," *Electronics Letters*, vol. 37, no. 23, pp. 1417–1418, 2001.

[17] P. Gilabert, G. Montoro, and E. Bertran, "On the wiener and hammerstein models for power amplifier predistortion," in *2005 Asia-Pacific Microwave Conference Proceedings*, vol. 2, 2005, pp. 1–4. DOI: 10.1109/APMC.2005.1606491.

[18] M. Schoukens and K. Tiels, "Identification of block-oriented nonlinear systems starting from linear approximations: A survey," *Automatica*, vol. 85, pp. 272–292, 2017. DOI: 10.1016/j.automatica.2017.06.044.

[19] M. Schetzen, *The Volterra and Wiener Theories of Nonlinear Systems*. New York, NY, USA: John Wiley & Sons, 1980, ISBN: 9780471044550.

[20] J. P. Martins, P. M. Cabral, N. B. Carvalho, and J. C. Pedro, "A metric for the quantification of memory effects in power amplifiers," *IEEE Transactions on Microwave Theory and Techniques*, vol. 54, no. 12, pp. 4432–4439, 2006. DOI: 10.1109/TMTT.2006.882871.

[21] H. Jiang and P. A. Wilford, "Digital predistortion for power amplifiers using separable functions," *IEEE Transactions on Signal Processing*, vol. 58, no. 8, pp. 4121–4130, 2010. DOI: 10.1109/TSP.2010.2049742.

[22] L. Ljung, *System Identification: Theory for the User*, 2nd ed. Prentice Hall PTR, 1999, ISBN: 9780136566953.

[23] R. Raich, H. Qian, and G. T. Zhou, "Orthogonal polynomials for power amplifier modeling and predistorter design," *IEEE Transactions on Vehicular Technology*, vol. 53, no. 5, pp. 1468–1479, 2004. DOI: 10.1109/TVT.2004.832415.

[24] A. N. Tikhonov and V. Y. Arsenin, *Solutions of Ill-Posed Problems*. Washington, DC, USA: Winston, 1977, ISBN: 9780470991244.

[25] A. E. Hoerl and R. W. Kennard, "Ridge regression: Biased estimation for nonorthogonal problems," *Technometrics*, vol. 12, no. 1, pp. 55–67, 1970.

[26] C. Rapp, "Effects of hpa-nonlinearity on a 4-dpsk/ofdm-signal for a digital sound broadcasting system," in *Proceedings of the Second European Conference on Satellite Communications*, ser. ESA SP-332, Liege, Belgium, 1991, pp. 179–184.

[27] Y. Wu, G. D. Singh, M. Beikmirza, L. C. N. de Vreede, M. Alavi, and C. Gao, "Opendpd: An open-source end-to-end learning & benchmarking framework for wideband power amplifier modeling and digital pre-distortion," in *2024 IEEE International Symposium on Circuits and Systems (ISCAS)*, 2024, pp. 1–5. DOI: 10.1109/ISCAS58744.2024.10558162.

[28] P. N. Landin and D. Rönnow, "Rf pa modeling considering odd-even and odd order polynomials," in *2015 IEEE Symposium on Communications and Vehicular Technology in the Benelux (SCVT)*, 2015, pp. 1–6. DOI: 10.1109/SCVT.2015.7374233.

[29] Y. Wu, A. Li, and C. Gao, *OpenDPDv2: A unified learning and optimization framework for neural network digital predistortion*, Under review, 2025. DOI: 10.48550/arXiv.2507.06849. arXiv: 2507.06849 [eess.SP].

[30] K. J. Muhonen, M. Kavehrad, and R. Krishnamoorthy, "Look-up table techniques for adaptive digital predistortion: A development and comparison," *IEEE Transactions on Vehicular Technology*, vol. 49, no. 5, pp. 1995–2002, 2000. DOI: 10.1109/25.892601.

[31] S. Ba, K. Waheed, and G. Zhou, "Efficient lookup table-based adaptive baseband predistortion architecture for memoryless nonlinearity," *EURASIP Journal on Advances in Signal Processing*, vol. 2010, p. 379 249, 2010. DOI: 10.1155/2010/379249.

[32] P. Jardin and G. Baudoin, "Filter lookup table method for power amplifier linearization," *IEEE Transactions on Vehicular Technology*, vol. 56, no. 3, pp. 1076–1087, 2007. DOI: 10.1109/TVT.2007.895566.

[33] P. L. Gilabert, A. Cesari, G. Montoro, E. Bertran, and J.-M. Dilhac, "Multi-lookup table fpga implementation of an adaptive digital predistorter for linearizing rf power amplifiers with memory effects," *IEEE Transactions on Microwave Theory and Techniques*, vol. 56, no. 2, pp. 372–384, 2008. DOI: 10.1109/TMTT.2007.914346.

[34] F. Zou, X. Liu, and X. Gu, "Memory effects in digital predistortion of twtas," in *2024 Joint International Vacuum Electronics Conference and International Vacuum Electron Sources Conference (IVEC + IVESC)*, 2024, pp. 1–2. DOI: 10.1109/IVECIVESC60838.2024.10694900.

[35] Y. Y. Woo et al., "Adaptive digital feedback predistortion technique for linearizing power amplifiers," *IEEE Transactions on Microwave Theory and Techniques*, vol. 55, no. 5, pp. 932–940, 2007. DOI: 10.1109/TMTT.2007.895145 .

[36] C. D. Presti, D. F. Kimball, and P. M. Asbeck, "Closed-loop digital predistortion system with fast real-time adaptation applied to a handset wcdma pa module," *IEEE Transactions on Microwave Theory and Techniques*, vol. 60, no. 3, pp. 604–618, 2012. DOI: 10.1109/TMTT.2011.2181860.

[37] A. S. Tehrani, "Behavioral modeling of wireless transmitters for distortion mitigation," Ph.D. dissertation, Department of Signals and Systems, Chalmers University of Technology, 2012. [Online]. Available: https://publications.lib.chalmers.se/records/fulltext/165106.pdf.

A

Appendix 1

In this appendix, the figures for the SSPA ACLR performance under the complexity reduction are presented.

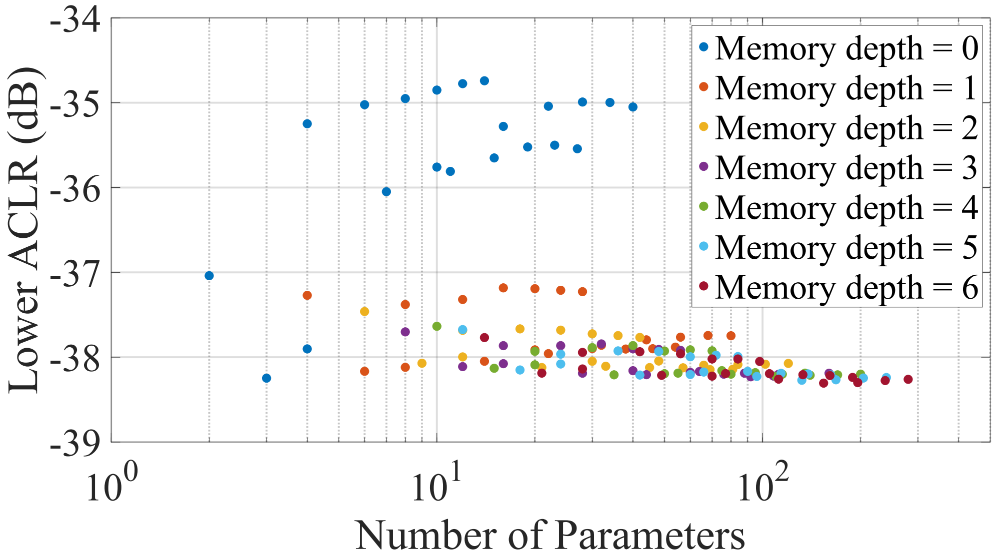

Figure A.1: Lower ACLR for the QPSK signal when performing the complexity reduction study.

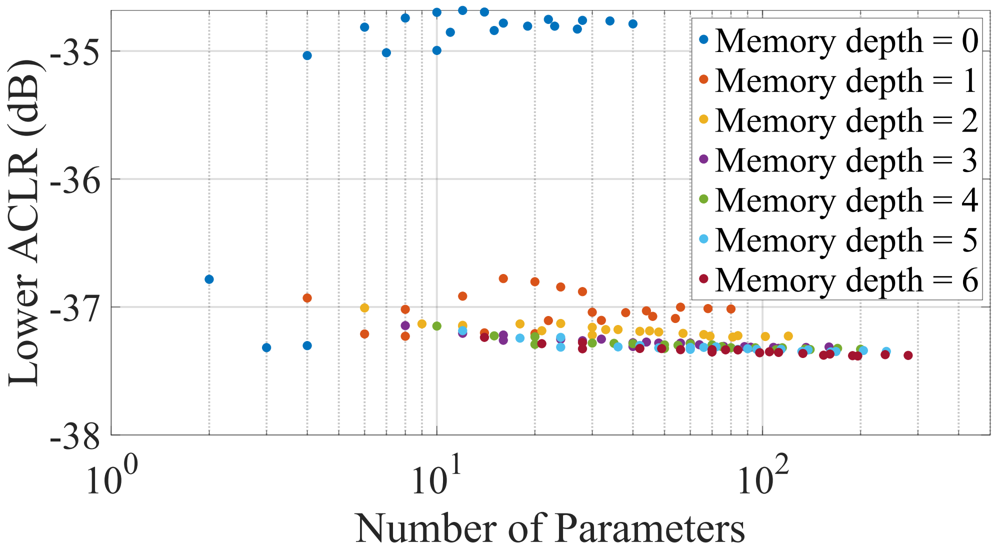

Figure A.2: Lower ACLR for the 16-QAM signal when performing the complexity reduction study.

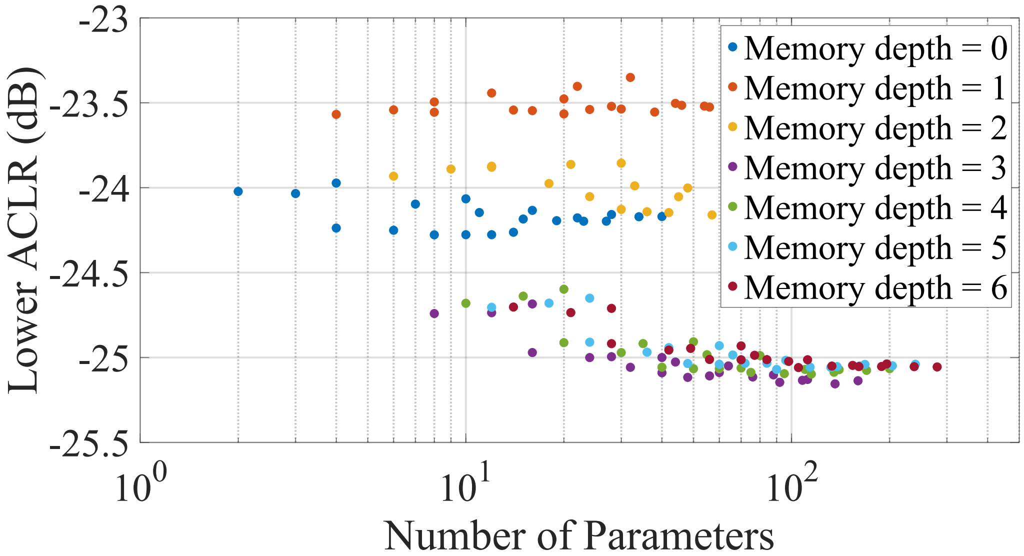

Figure A.3: Lower ACLR for the DFT-s-OFDM signal when performing the complexity reduction study.

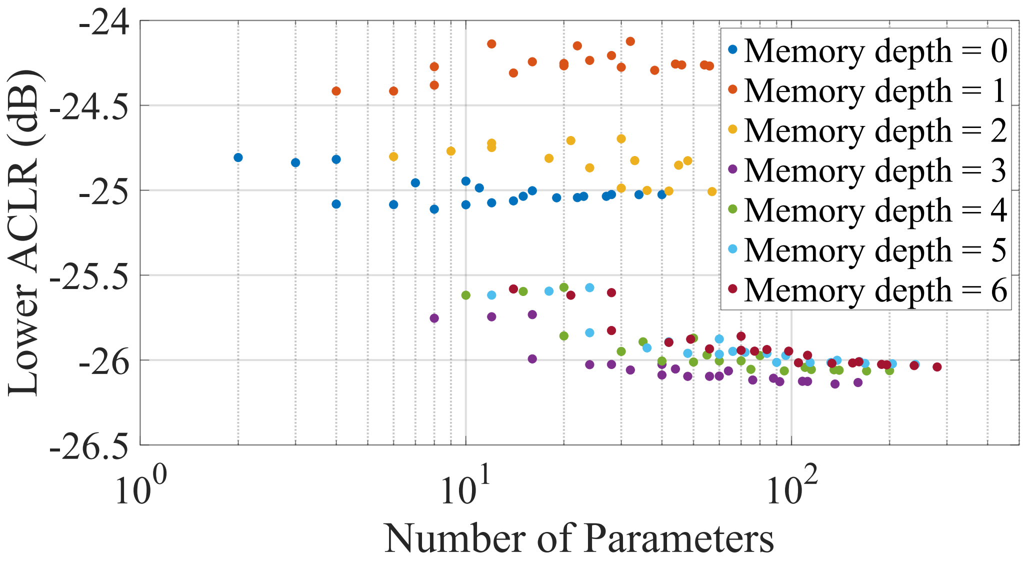

Figure A.4: Lower ACLR for the CP-OFDM signal when performing the complexity reduction study.

DEPARTMENT OF Electrical Engineering
CHALMERS UNIVERSITY OF TECHNOLOGY
Gothenburg, Sweden 2026
www.chalmers.se

CHALMERS
UNIVERSITY OF TECHNOLOGY